

# *Recent decadal changes in heat waves over China: drivers and mechanisms*

Article

Accepted Version

Su, Q. and Dong, B. ORCID: <https://orcid.org/0000-0003-0809-7911> (2019) Recent decadal changes in heat waves over China: drivers and mechanisms. *Journal of Climate*, 32 (14). pp. 4215-4234. ISSN 1520-0442 doi: <https://doi.org/10.1175/JCLI-D-18-0479.1> Available at <https://centaur.reading.ac.uk/83196/>

It is advisable to refer to the publisher's version if you intend to cite from the work. See [Guidance on citing](#).

To link to this article DOI: <http://dx.doi.org/10.1175/JCLI-D-18-0479.1>

Publisher: American Meteorological Society

All outputs in CentAUR are protected by Intellectual Property Rights law, including copyright law. Copyright and IPR is retained by the creators or other copyright holders. Terms and conditions for use of this material are defined in the [End User Agreement](#).

[www.reading.ac.uk/centaur](http://www.reading.ac.uk/centaur)

**CentAUR**

Central Archive at the University of Reading

Reading's research outputs online



1           **Recent decadal changes in heat waves over China: drivers and**  
2                                   **mechanisms**

3                                           Su Qin<sup>1</sup> and Buwen Dong<sup>2</sup>

4

5     <sup>1</sup> Department of Atmospheric Sciences, Yunnan University, Kunming, China

6     <sup>2</sup> National Centre for Atmospheric Science-Climate, Department of Meteorology,  
7     University of Reading, Reading, UK

8

9

10

11

12

13

14

15

16

17

18

19

20

21   Corresponding author:

22   Qin Su,

23   Department of Atmospheric Sciences,

24   Yunnan University,

25   Kunming, 650091, China

26   E-mail: suqin@ynu.edu.cn

27

28 **Abstract**

29 Observational analysis indicates significant decadal changes in daytime, nighttime,  
30 and compound (both daytime and nighttime) heat waves (HWs) over China across the  
31 mid-1990s, featured by the rapid increase in frequency, intensity, and spatial extent.  
32 The spatial variations of these observed decadal changes are assessed by the  
33 comparison between the present day (PD) of 1994-2011 and the early period (EP) of  
34 1964-1981. The compound HWs change most remarkably in all three aspects, with  
35 frequency averaged over China in the PD tripling that in the EP and both intensity and  
36 spatial extent nearly doubling. The daytime and nighttime HWs also change  
37 significantly in all three aspects.

38 A set of numerical experiments is used to investigate the drivers and physical  
39 processes responsible for the decadal changes of the HWs. Results indicate the  
40 predominant role of the anthropogenic forcing, including changes in greenhouse gas  
41 (GHG) concentrations and anthropogenic aerosol (AA) emissions in the decadal  
42 changes of the HWs. The GHG changes have dominant impacts on the three types of  
43 HWs, while the AA changes make significant influences on daytime HWs. The GHG  
44 changes increase the frequency, intensity, and spatial extent of the three types of HWs  
45 over China both directly via the strengthened Greenhouse Effect and indirectly via land-  
46 atmosphere and circulation feedbacks in which GHG-change-induced warming in sea  
47 surface temperature plays an important role. The AA changes decrease the frequency  
48 and intensity of daytime HWs over Southeastern China through mainly aerosol-  
49 radiation interaction, but increase the frequency and intensity of daytime HWs over

50 Northeastern China through AA-change-induced surface-atmosphere feedbacks and  
51 dynamical changes related to weakened East Asian summer monsoon.

## 52 **1. Introduction**

53 Heat waves, commonly defined as prolonged period of excessive hot weather, are a  
54 distinctive type of high temperature extremes (Perkins and Alexander 2013, Perkins  
55 2015). These high-temperature extremes show increasing occurrence in recent decades  
56 as the global mean temperature rises (e.g., Alexander et al. 2006; Donat et al. 2013),  
57 leading to severe damages to the human society and ecosystems (e.g. Meehl and Tebaldi  
58 2004; Fischer et al. 2007; Coumou and Rahmstorf 2012; Seneviratne et al. 2014; Sun  
59 et al. 2014). For instance, the extreme long-lasting heat wave over Europe during the  
60 summer of 2003 caused about 66 000 deaths (e.g. Schär and Jendritzky 2004; Robine  
61 et al. 2008) and the record-breaking heat wave over western Russia during July of 2010  
62 yielded a death toll of 11 000 and grain-harvest losses of 30% (e.g. Coumou and  
63 Rahmstorf 2012; Matsueda 2011). The disastrous impact of heat waves on the human  
64 lives, agriculture, and economies highlights the urgency of understanding the changes  
65 of heat waves and associated physical processes.

66 Since the mid-1990s, heat waves have become more frequent and severe across  
67 China (You et al. 2017; Li et al. 2017; Luo and Lau 2017; Wang et al. 2017, Freychet  
68 et al. 2018a). Several devastating heat waves in recent decades, such as the 2013 July-  
69 August heat wave in Central and Eastern China and the 2015 summer heat wave in  
70 Western China have caused considerable damages to agricultural production and human

71 health (e.g. Sun et al. 2016; Ma et al. 2017). The 2013 July-August heat wave in Central  
72 and Eastern China lasted more than 30 days (Zhou et al. 2014; Ma et al. 2017) and the  
73 regionally averaged surface air temperature broke the historical record, exceeding the  
74 observed 1961–1990 climatology by 1.89 °C. The 2015 summer registered the hottest  
75 summer over western China, with the area-averaged summer daily mean, maximum,  
76 and minimum surface air temperatures breaking the historical records (Sun et al. 2016).  
77 In addition, Northeast China experienced a hot summer in 2014, which is associated  
78 with decrease in precipitation (Wilcox et al. 2015a).

79 Previous studies demonstrated a crucial role of anthropogenic activity in increasing  
80 the occurrence of the extreme temperatures and long-lasting heat waves over China  
81 (Wen et al. 2013; Sun et al. 2014; Lu et al. 2016; Freychet et al. 2017; 2018a, b; Chen  
82 and Dong 2018), as well as intensifying the magnitude of the extreme temperatures  
83 (Yin et al. 2017). Most of those studies focused on all combined anthropogenic impact,  
84 rather than the individual effect of anthropogenic forcing. For instance, the individual  
85 role of changes in greenhouse gases concentrations (GHG) and anthropogenic aerosol  
86 (AA) emissions in the changes of long-lasting heat waves are not clear.

87 Different anthropogenic forcings influence the atmospheric temperature through  
88 distinct thermodynamic and dynamical processes, but the mechanisms related to the  
89 responses of HWs to different anthropogenic forcings have not been fully understood  
90 yet. The increase in GHG concentrations warms the atmosphere by absorbing more  
91 outgoing longwave radiation (e.g., Cubasch et al. 2001; Dong et al. 2009). At the same  
92 time, the atmospheric temperature are also affected by the circulation changes due to

93 the GHG concentration changes. The increased GHG concentrations enhance the  
94 southern part of East Asia Summer Monsoon (EASM) circulation, which results from  
95 the competing effects of the increase in moisture static energy related to the  
96 strengthened land-sea thermal contrast and the mid-troposphere convective barrier  
97 associated with the reduced relative humidity in a warming world (Lau and Kim 2017;  
98 Lau et al. 2017). In addition, the strengthened land-sea thermal contrast is determined  
99 by the direct GHG radiative effect (Li and Ting 2017, Tian et al. 2018). The changes of  
100 AA emissions affect the surface and atmospheric temperature by directly scattering and  
101 absorbing the solar radiation through aerosol-radiation interaction and by changing the  
102 cloud properties through aerosol-cloud interaction (e.g. Rosenfeld et al. 2008; Stevens  
103 and Feingold 2009; Tao et al. 2012; Li et al. 2016b). Not only the local AA emission  
104 changes, but also the remote AA emission changes have an impact on the summer  
105 extreme temperatures over China through aerosol change induced precipitation-soil  
106 moisture-cloud-temperature feedbacks (Dong et al. 2016a; 2016b). Local summer  
107 warming associated with reduced precipitation leads to decrease in evaporation and less  
108 cloud cover since precipitation deficit induces drying soil. Increased solar radiation at  
109 the surface associated with less cloud cover and decreased upward latent heat fluxes  
110 associated with reduced evaporation cause a positive feedback to the surface warming.  
111 Moreover, the dynamical feedbacks of reduced the EASM circulation and rainfall,  
112 which induced by the weakened land-sea thermal contrast and more stable atmosphere  
113 in response to the increase in AA emissions, could also have an impact on atmospheric  
114 temperature (Guo et al. 2013, Li et al. 2016b; Li et al. 2018b, Tian et al. 2018).

115 Up to now, the heat waves are precisely classified into three categories (e.g., Chen  
116 and Li 2017; Chen and Zhai 2017): daytime (only hot in day), nighttime (only hot at  
117 night), and compound ones (hot in both day and night), since extreme high temperature  
118 at night, inducing great heat-related morbidity and mortality (Hajat et al. 2006; Gosling  
119 et al. 2009), is noticed as disastrous as that in daytime. These three types of heat waves  
120 are of different features and associated with different mechanisms (e.g. Chen and Li  
121 2017; Chen and Zhai 2017; Hong et al. 2018). However, most of the previous studies  
122 focused on the characteristics and changes of daytime heat waves (e.g., Ding et al. 2010;  
123 Guo et al. 2017; Luo and Lau 2017; Lu and Chen 2016; Wang et al. 2017). The changes  
124 of compound and nighttime heat waves, especially drivers and physical mechanisms  
125 for the recent decadal change, are not well understood (You et al. 2017; Li et al. 2017,  
126 Luo and Lau 2017). Also, the individual contributions of changes in GHG  
127 concentrations and AA emissions to the recent decadal changes in heat waves are not  
128 evaluated and the associated physical processes are not revealed yet, since the previous  
129 studies assessed all anthropogenic impacts together (e.g., Sun et al. 2016; Ma et al.  
130 2017). Therefore, the main aims of this work are to revisit the time evolutions in the  
131 three types of heat waves over China in observations with a focus on the recent decadal  
132 changes across the mid-1990s, to quantify the relative roles of changes in GHG  
133 concentrations and AA emissions in shaping these decadal changes, and to understand  
134 the associated physical processes.

135 The structure of this paper is organized as follows: The observed decadal changes in  
136 heat waves over China are revisited in Section 2. The model and experiments are



137 described briefly in Section 3. The simulated changes in response to different changes  
138 in anthropogenic forcings are shown in Section 4. The physical processes responsible  
139 for simulated changes in heat waves forced by different anthropogenic forcings, such  
140 as GHG concentrations and AA emissions, are illustrated in Section 5. Conclusions are  
141 summarized in Section 6.

## 142 **2. Observed decadal changes in heat waves over China**

### 143 **2.1 Observational datasets**

144 Observations used in this are the homogenized datasets of daily maximum  
145 temperature (Tmax) and minimum temperature (Tmin) in 753 stations over China  
146 during 1960-2013 (Li et al. 2016a). Regarding to distinct local climate in China, the  
147 HWs over three sub-regions are also analyzed, which are Southeastern China (SEC,  
148 south of 35°N and east of 105°E), Northeastern China (NEC, north of 35°N and east of  
149 105°E), and Western China (WC, west of 105°E). There are 334, 224, and 195 stations  
150 in SEC, NEC, and WC, respectively. Fig. 2g shows the distributions of the stations over  
151 these three sub-regions. This study focuses on the extended summer (May–September)  
152 HWs.

### 153 **2.2 Definition of HWs**

154 A HW is defined as a weather event with daily temperature exceeding a threshold  
155 continuously for a few days (e.g., Perkins and Alexander 2013). Both absolute and  
156 relative thresholds could be used to define a heat wave. The absolute threshold is a fixed  
157 temperature value, such as 35°C (e.g., Tan et al. 2007; Sun et al. 2014), while the

158 relative threshold is decided by local climate, varying at different places on different  
159 dates (Stefanon et al. 2012). Concerning the various climate types in China, the relative  
160 threshold is employed to define the heat waves in this study and it has also been widely  
161 used in some previous studies (e.g., Li et al. 2017; Wang et al. 2017). The relative  
162 threshold on each calendar day is calculated as the daily 90<sup>th</sup> percentile of Tmax or  
163 Tmin based on 15-day samples centered on that day during the baseline period of 1964-  
164 1981 (i.e. total samples 15\*18 = 270 days, Della-Marta et al. 2007). A HW is defined  
165 when the daily temperature is higher than the relative threshold for at least three days.  
166 All the HWs are categorized to three independent types:

- 167 (1) compound HW - at least **three** consecutive days with simultaneous hot days and  
168 hot nights ( $T_{max} \geq 90^{\text{th}}$  percentile and  $T_{min} \geq 90^{\text{th}}$  percentile).
- 169 (2) daytime HW - at least **three** consecutive hot days (only  $T_{max} \geq 90^{\text{th}}$  percentile),  
170 without consecutive hot nights.
- 171 (3) nighttime HW - at least **three** consecutive hot nights (only  $T_{min} \geq 90^{\text{th}}$  percentile),  
172 without consecutive hot days.

173 Three indicators, i.e. frequency, intensity, and spatial extent, are used to measure the  
174 HWs in a year. The frequency is represented by the accumulated occurrence of events  
175 within a year. The intensity of each event is calculated by averaging the everyday  
176 temperature anomalies within an event, which are obtained by subtracting the  
177 corresponding threshold from the daily temperatures. Particularly, the intensity of  
178 compound HWs is the sum of the averaged Tmax and Tmin anomalies. The intensity

179 for a year is computed by averaging the intensity of events occurring in that year. The  
180 spatial extent is calculated through a “frozen grid” scheme (Jones et al., 1986). The  
181 mainland of China is divided into  $1.875^\circ$  longitude  $\times$   $1.25^\circ$  latitude boxes, with a total  
182 number of  $N$ . There are  $n(i)$  stations in total situated in box  $i$ , in which  $nh(i, t)$  stations  
183 experience at least one extreme event during the extended summer in year  $t$ . Then the  
184 spatial extent in year  $t$  is computed as  $\sum_{i=0}^{i=N} \frac{nh(i,t)}{n(i)} \times 1.875 \times 110 \times 1.25 \times 110$ , in  
185 which “110” denotes an approximate distance per unit longitude/latitude.

### 186 **2.3 Observed decadal change**

187 Figure 1 shows the time evolution of the area averaged frequency and intensity as  
188 well as the spatial extent of the compound, daytime, and nighttime HWs. The timeseries  
189 of the three properties of compound and nighttime HWs seems to be dominated by  
190 linear trends on low frequency time scale, while those of daytime HWs are featured by  
191 abrupt decadal changes. These could be attributed to that the changes in compound and  
192 nighttime HWs are predominantly contributed to by the changes of GHG  
193 concentrations, which show an increasing trend (Le Quere et al. 2009), and the changes  
194 in daytime HWs are partly influenced by the AA changes, which show significant  
195 decadal changes across mid-1990s (Lamarque et al. 2010), which are indicated by the  
196 results in section 4. What is interesting, the frequency and intensity of one type of HWs  
197 are highly correlated with the correlation coefficient for whole China of 0.90, indicating  
198 highly coupled interannual variations of frequency and intensity of one type of HWs.  
199 However, the interannual variations is not the concern of this study, which would not  
200 be explored more in this paper.

201 All three type HWs over China experienced an abrupt decadal change across the mid-  
202 1990s, characterized by increases in frequency, intensity, and spatial extent (Figure 1).  
203 These rapid decadal changes are robust features and they are not sensitive to the  
204 baseline period used to find the relative thresholds and define HWs. In the rest of this  
205 paper, HWs are defined using the relative thresholds based on the period of 1964-1981.  
206 Comparing to daytime and nighttime HWs, compound HWs exhibited the most  
207 dramatic changes in all three aspects. The frequency of compound HWs during 1994-  
208 2011 (present day, PD hereafter) almost tripled that during 1964-1981 (early period, EP  
209 hereafter), rising from 0.67 events per year to 1.85 events per year (Table 2). These two  
210 periods were chosen to avoid years with a strong impact of the volcanic eruptions (Dong  
211 et al. 2017). The intensity of compound HWs doubled the value of the EP after mid-  
212 1990s, with the value changing from 1.42 °C to 3.09 °C (Table 2). The spatial extent of  
213 compound HWs expanded from  $3.66 \times 10^6$  km<sup>2</sup> to  $6.97 \times 10^6$  km<sup>2</sup> (Table 2). The decadal  
214 changes of daytime HWs show some similar features in comparison with the compound  
215 ones, but with relatively small magnitude. The frequency and intensity of daytime HWs  
216 increased by 0.7 events per year and 0.29 °C (Table 2). The spatial extent expanded  
217 from  $8.38 \times 10^6$  km<sup>2</sup> to  $8.86 \times 10^6$  km<sup>2</sup> (Table 2), in comparing with the whole China area  
218 of  $9.63 \times 10^6$  km<sup>2</sup>. The nighttime HWs also showed decadal increases in all three aspects.  
219 The frequency of nighttime HWs exhibited a sharp increase across mid-1990s,  
220 changing from 1.76 events per year to 3.72 events per year, which means that there are  
221 averaged two more nighttime HWs over China in every summer during the PD relative  
222 to the EP (Table 2). The intensity of nighttime HWs enhanced significantly by 0.41 °C

223 (Table 2). The influencing area increased by about 20% (Table 2). In addition, the  
224 frequency and intensity of the three types of HWs averaged over the three sub-regions  
225 show similar rapid decadal changes as those averaged over whole China. Moreover, all  
226 the area averaged changes above are calculated based on station data. The area averaged  
227 changes are also computed after interpolating station data to regular grids and they are  
228 nearly identical to the ones based on station data.

229 Figure 2 illustrates the spatial patterns of the decadal changes in frequency and  
230 intensity of the three types of HWs over China across the mid-1990s in observations.  
231 Nearly all the decadal changes in each indicator of three type HWs are positive  
232 throughout China, but with different spatial patterns. The occurrence of compound  
233 HWs increased the most over the northern part of China, mid-lower Reaches of the  
234 Yangtze River, and the Delta of the Pearl River, with an increase in frequency more  
235 than 2.0 events per year (Fig. 2a). The changes of intensity of compound HWs share a  
236 similar spatial distribution with the frequency (Fig. 2b), with the maximum of intensity  
237 changes located at the northern part of China (about 4.8 °C). The spatial patterns of  
238 changes in frequency and intensity for daytime and nighttime HWs show some distinct  
239 features with increases in both frequency and intensity for nighttime HWs being  
240 stronger than those for daytime HWs (Fig. 2c-f). The significant increase of frequency  
241 of daytime HWs primarily appeared in the northern part of China, especially in the  
242 western part of China with the value of about 2.5 events per year (Fig. 2c), while the  
243 significant intensification in magnitude of daytime HWs around 0.6 °C mainly occurred  
244 in the central part of China (Fig. 2d). The frequency of nighttime HWs increased

245 significantly in the northern part of China (Fig. 2e), with a range of 1.5 to 3.0 events  
246 per year. The largest increase is situated on the south flank of the Tibetan Plateau with  
247 the maximum of 6.2 events per year. The intensity of the nighttime HWs significantly  
248 enhanced in the northern part of China (Fig. 2f), with the maximum of 1.1 °C.  
249 Interestingly, the nighttime HWs in the central-eastern China exhibited large increase  
250 in frequency and intensity, while the daytime HWs over there showed the opposite  
251 changes, with frequency decreasing and intensity weakening slightly and the compound  
252 HWs over there displayed little changes. Previous studies investigating the linear trends  
253 of the HWs also reported similar changes in these three types of HWs in the central-  
254 eastern China (Ding et al. 2010; Chen and Li 2017; Freychet et al. 2017). However, the  
255 physical mechanism for the trends in these three type HWs is still not clear.

### 256 **3. Model and experiments design**

257 The above results show that the observed three types of HWs exhibited significant  
258 decadal changes across the mid-1990s. A set of numerical experiments is performed to  
259 assess whether the anthropogenic forcings (GHG concentrations and AA emissions)  
260 contribute to these decadal changes in observations, and what the relative roles of  
261 individual forcing are, and what the main physical processes involved are.

#### 262 **3.1 Model and experiments design**

263 This study used an atmosphere-ocean-mixed-layer coupled model, MetUM-GOML1  
264 (Hirons et al. 2015) by performing a set of numerical experiments, to estimate the  
265 contributions of combined GHG and AA changes or individual forcing change on the

266 decadal changes of three type HWs in China. MetUM-GOML1 is a coupled model  
267 comprising of the atmosphere component of the Met Office Unified Model at the fixed  
268 scientific configuration Global Atmosphere 3.0 (GA3.0; Arribas et al. 2011; Walters et  
269 al. 2011) and a Multi-Column K Profile Parameterization (MC-KPP) mixed-layer ocean  
270 model. The vertical MC-KPP columns are configured over 100 levels within a depth of  
271 1000 m using a stretch function, so the vertical resolution of MC-KPP is 1.2m at the  
272 surface and about 2 m over the first 41.5 m near the surface. Since MC-KPP includes  
273 only vertical mixing processes and does not include ocean dynamics, the corrections of  
274 temperature and salinity are applied. In the corrections, the mean ocean advections are  
275 represented by the prescribed seasonally-varying 3-dimension temperature and salinity  
276 fluxes, which also account for the biases in atmospheric surface heat and fresh water  
277 fluxes. The frequency of coupling between atmospheric and oceanic components is  
278 once every three hours. The advantages of this atmosphere-ocean-mixed-layer coupled  
279 model are less computational time and smaller biases in simulated sea surface  
280 temperature than the fully coupled ones (Hirons et al. 2015, Dong et al. 2017; Luo et  
281 al. 2018). All experiments are run at the horizontal resolution of  $1.875^\circ$  longitude by  
282  $1.25^\circ$  latitude with 85 vertical levels in the atmosphere.

283 Table 1 summarized the performed experiments in this study. First of all, a relaxation  
284 experiment (R0) for 12 years was performed. In relaxation experiment, the PD GHG  
285 and AA forcings (Lamarque et al. 2010; 2011) are used and the ocean temperature and  
286 salinity were relaxed to a PD (1994-2011) climatology, which is derived from the Met  
287 Office ocean analysis (Smith and Murphy, 2007). The climatological seasonal cycle of

288 daily mean 3D ocean temperature and salinity corrections are obtained from the  
289 relaxation experiment. These ocean temperature and salinity corrections are then  
290 applied to the free-running coupled experiments. Four other time-sliced experiments  
291 are performed by using different forcings, i.e. C-EP experiment forced by the EP  
292 (1964–1981) mean GHG concentrations and appropriate AA emissions, C-PD  
293 experiment forced by the PD (1994–2011) mean GHG concentrations and AA  
294 emissions, C-PD-GHG experiment forced by the PD mean GHG concentrations, but  
295 the appropriate EP mean AA emissions, C-PD-AA experiment forced by the PD mean  
296 AA emissions, but the EP mean GHG concentrations. All experiments are run for 50  
297 years and use the climatological PD sea ice extent from HadISST (Rayner et al. 2003).  
298 The same set of experiments was used to investigate the forced decadal summer  
299 precipitation change over East Asia in Tian et al. (2018) and the decadal changes of  
300 temperature extremes over China in Chen and Dong (2018). The last 45 years of each  
301 experiment are used for analysis. The HWs in the experiments are defined by the same  
302 way as in observations, expect that the relative threshold on each day is calculated as  
303 the daily 90<sup>th</sup> percentile of Tmax or Tmin based on 15-day samples centered on this day  
304 during the last 45 years of C-EP experiment (i.e. total samples  $15 \times 45 = 675$  days). The  
305 difference between a pair of experiments that include and exclude a particular forcing  
306 indicates the response to that forcing. The difference between C-PD and C-EP indicates  
307 the combined effect of changes in both GHG concentrations and AA emissions  
308 (hereafter ALL forcing). The impact of changes in GHG concentrations (hereafter GHG  
309 forcing) is the difference between C-PD-GHG and C-EP and the impact of changes in



310 AA emissions (hereafter AA forcing) is the difference between C-PD-AA and C-EP.  
311 Statistical significance of the mean changes are assessed using a two tailed Student *t*-  
312 test.

### 313 **3.2 Model climate for Tmax and Tmin**

314 The climatological means of Tmax and Tmin in the C-PD experiment for the  
315 extended summer are compared with the observed ones during PD (Fig. 3). The  
316 observed Tmax means show more or less uniform distributions over the southeastern  
317 part of China with value higher than 29 °C, decreasing northward with value about 23-  
318 26°C over the northeastern part of China. Over western China, a low value centre is  
319 located over the Tibetan Plateau and a high value centre over northwestern part of China  
320 with temperature above 29 °C (Fig. 3a). The climatological means of observed Tmin  
321 exhibit great meridional gradient over eastern part of China with the maximum higher  
322 than 23 °C in southeast coast of China and minimum of 8-11°C over Northeast China.  
323 The spatial distribution of Tmin over western China shows a minimum (less than 2°C)  
324 over the Tibetan Plateau and a high value (14-20°C) over northwestern part of China,  
325 being similar to spatial pattern in Tmax (Fig. 3b). The spatial patterns of climatological  
326 extended summer means of Tmax and Tmin in the C-PD experiment and regional  
327 magnitudes agree well with the observed ones with pattern correlation coefficients of  
328 0.82 for Tmax and 0.88 for Tmin (Fig. 3c and d). The observed Tmax distributions are  
329 reproduced by the model over southeastern and northwestern part of China with value  
330 above 29 °C, but slightly underestimated over the Tibetan Plateau and northeastern part  
331 of China (Fig. 3d). The observed Tmin distributions are also well simulated by the

332 model, with some underestimation over the Tibetan Plateau (Fig. 3c). These results  
333 indicate that the model reproduce many features of the extended summer climatological  
334 means of Tmax and Tmin in observations, suggesting that the model used in this study  
335 is appropriate for investigating the response of the temperature extremes related HWs  
336 to different anthropogenic forcings.

#### 337 **4. Model simulated responses to different anthropogenic forcings**

##### 338 **4.1 Spatial pattern of responses to different forcings**

339 Figure 4 shows the spatial patterns of changes in frequency and intensity of the  
340 compound HWs in response to different anthropogenic forcings in model experiments.  
341 The significant increases in the frequency and intensity throughout China and their  
342 spatial distributions in observations (Fig. 2a and b) are well reproduced by the ALL  
343 forcing experiment (Fig. 4a and b). The spatial patterns of the increases in the model  
344 experiment are consistent with the observed ones with relatively large increase in  
345 frequency and strong enhancement in intensity over the northern part of China and mid-  
346 lower Reaches of Yangtze River, though the magnitudes of the changes in response to  
347 ALL forcing for increases in frequency are smaller than the observed ones. These  
348 results demonstrate that the observed decadal increases in occurrence and intensity of  
349 compound HWs over China across the mid-1990s are predominantly attributed to the  
350 anthropogenic GHG and AA changes.

351 Furthermore, the changes of compound HWs in response to GHG forcing share very  
352 similar patterns with the changes in the ALL forcing experiment (Fig. 4c and d), while

353 the changes driven by the AA forcing are relatively weak, except of some local  
354 significant decreases in frequency and intensity over SEC (Fig. 4e and f). Thus,  
355 comparing the responses to only GHG with those to only AA changes indicates that the  
356 GHG changes play a dominant role in the increase in frequency and intensity of  
357 compound HWs. In addition, the model overestimates the increase in frequency of  
358 compound HWs over the southwestern part of China, which is resulted from the GHG  
359 impact (Fig. 2a and Fig. 4a and c).

360 The changes of daytime HWs in response to the different forcings are shown in figure  
361 5. The principle features of the changes of daytime HWs in the ALL forcing experiment  
362 are significant increases in frequency and intensity over the northern part of China (Fig.  
363 5a and b). These main features show some similarities with the observed changes (Fig.  
364 2c and d). However, the changes in the intensity of daytime HWs over the northern part  
365 of China are overestimated, but those over the central part of China are underestimated.  
366 Both the GHG and AA forcing changes are important to the changes of daytime HWs.  
367 Responses to the GHG forcing share the similar spatial patterns with those in the ALL  
368 forcing experiment, with a little difference in the magnitude of changes, indicating the  
369 dominant role of GHG changes in affecting the daytime HWs (Fig. 5c and d). Changes  
370 of the daytime HWs induced by the AA impact exhibit dipole patterns over China with  
371 increases over northern China and decreases or weak changes over southern China (Fig.  
372 5e and f). In addition, the responses to AA forcing are of more significance for daytime  
373 HWs than for compound HWs, implying greater AA impact on the daytime HWs.

374 Responses of the nighttime HWs to the different forcings are shown in figure 6. In

375 comparison with observed changes shown in Fig. 2, the model reproduces significant  
376 increases in the frequency and intensity of the nighttime HWs over the northern part of  
377 China in response to ALL forcing changes (Fig. 6a and b). Comparison between  
378 responses to different forcings illustrates that the significant changes of the nighttime  
379 HWs in the model simulations are primarily due to the GHG changes (Fig. 6c and d)  
380 with impacts of changes in AA being generally weak (Fig. 6e and f). Additionally, the  
381 increases in frequency over the southeastern part of China are overestimated, because  
382 the GHG changes induce strong increases over there but the AA changes result in weak  
383 decreases.

#### 384 **4.2 Area averaged responses to different forcings**

385 The area averaged changes in frequency and intensity and changes in spatial extent  
386 of the three types of HWs over whole China and all three sub-regions for both  
387 observations and model experiments are demonstrated in Figure 7. Quantitatively, the  
388 changes of the three types of HWs in response to ALL forcing changes simulated by  
389 models are in some agreement with observations, not only over China as a whole, but  
390 also over the individual sub-regions, though the magnitudes of the changes in the model  
391 are slightly different from the observed ones.

392 For the compound HWs, in response to ALL forcing, the area averaged changes in  
393 frequency and intensity over the whole mainland China are 0.75 events per year and  
394 1.07 °C, which are about 2/3 of the observed 1.18 events per year and 1.67 °C (Fig. 7a  
395 and b), and the change in spatial extent over whole China is  $3.54 \times 10^6 \text{ km}^2$ , very close

396 to the  $3.31 \times 10^6$  km<sup>2</sup> in observations (Fig. 7c). Moreover, the simulated increases in  
397 frequency (intensity) averaged over the SEC and WC are very similar to the observed  
398 changes, but increases in frequency (intensity) over the NEC are weaker than  
399 observed changes. The simulated changes in spatial extent over the three sub-regions  
400 are also consistent with observations. Furthermore, the changes of GHG explain most  
401 responses in the simulated changes of compound HWs over whole China or over the  
402 three sub-regions, indicating the predominant role of GHG changes in affecting the  
403 compound HWs.

404 For the daytime HWs, the changes in frequency and intensity averaged over whole  
405 China and the three sub-regions in the ALL forcing experiment are close to those in the  
406 observations, with simulated changes over whole China of 0.93 events per year and  
407 0.38 °C relative to the observed ones of 0.70 events per year and 0.29 °C (Fig. 7d and  
408 e). The simulated change in spatial extent is overestimated (Fig. 7f). Similar with the  
409 compound HWs, the area averaged changes of the daytime HWs are primarily induced  
410 by the GHG changes. However different from the compound HWs, the changes of  
411 daytime HWs over the NEC and SEC are significantly influenced by the AA changes.  
412 The changes in frequency and intensity of daytime HWs over the NEC in response to  
413 AA forcing are 0.35 events per year and 0.15 °C, while they are -0.28 events per year  
414 and -0.12 °C over the SEC. These significant increases over the NEC and decreases  
415 over the SEC are consistent with the dipole pattern of AA induced changes in frequency  
416 and intensity (Fig. 5e and f).

417 For nighttime HWs, the simulated changes in most aspects agree well with the

418 observed ones except the change in frequency over NEC and the GHG changes play a  
419 key role in leading to the changes in frequency, intensity and spatial extent. The changes  
420 in frequency and intensity of nighttime HWs averaged over whole China in response to  
421 ALL forcing are 1.66 events per year and 0.36 °C, close to 1.96 events per year and  
422 0.41 °C in observations (Fig 7g and h). The simulated change in spatial extent is greater  
423 than the observed changes in whole region, SEC, and WC (Fig. 7i).

424 There is some nonlinearity for the changes in frequency and intensity for all three  
425 type HWs, especially strong for daytime HWs over the SEC in response to GHG and  
426 AA changes in model simulations, evidenced by the sum of the responses to separate  
427 GHG and AA forcing being not equal to the response to the ALL forcing. The  
428 nonlinearity is weak for changes of daytime HWs averaged over whole China and over  
429 other two sub-regions and all the area averaged changes of compound and nighttime  
430 HWs. The nonlinearity of responses to different forcings has noticed by previous  
431 studies (Feichter et al. 2004, Ming and Ramaswamy 2009, Shiogama et al. 2012).  
432 However, detailed discussion of this nonlinearity is beyond the scope of this study.

433 The results above indicate that the observed decadal changes in the frequency,  
434 intensity and spatial extent of compound, daytime, and nighttime HWs over China  
435 across the mid-1990s are primarily forced by the changes in anthropogenic forcings,  
436 such as GHG concentrations and AA emissions. The impact of GHG changes and that  
437 of AA changes are different in many aspects. GHG changes contribute dominantly to  
438 the increases in all aspects of the three types of HWs over most regions in China, while  
439 AA changes significantly increase the frequency and intensity of the daytime HWs over

440 NEC, but decrease them over SEC.

## 441 **5. Physical processes responsible for the simulated decadal changes of HWs**

442 The physical processes responsible for the decadal changes of the three types of HWs  
443 in response to different forcings are discussed in this section by diagnosing the seasonal  
444 mean responses. The changes of HWs could be contributed by the changes in the  
445 climatological seasonal mean temperature and the changes in temperature variability.  
446 The contribution of changes in variability is estimated by calculating the properties of  
447 three types of HWs in the C-PD simulation by removing the climatological extended-  
448 summer Tmax and Tmin differences between the C-PD and C-EP simulations relative  
449 to C-EP simulation and by comparing these new estimated changes with changes  
450 diagnosed from original C-PD simulation relative to C-EP simulation. Results indicate  
451 that removing the climatological mean state change nearly eliminate changes (not  
452 shown) in all properties of three type HWs over China seen in response to ALL forcing.  
453 These indicate little contribution of changes in temperature variability and suggest that  
454 the decadal changes of the three types of HWs in response to ALL forcing are  
455 predominantly attributed to the changes in the climatological seasonal mean  
456 temperature between C-PD and C-EP simulations. This conclusion is in agreement with  
457 Argueso et al. (2016) who showed that seasonal mean temperature changes control  
458 future heatwaves in most regions globally. Therefore, it is reasonable to examine the  
459 changes in the climatological seasonal mean state to discuss the associated physical  
460 processes.

## 461 **5.1 Induced by GHG forcing**

462 The spatial patterns of extended-summer-mean changes of some key variables in  
463 response to GHG changes are illustrated in Figure 8. The increased downward clear sky  
464 surface LW radiation ( $6.01 \text{ W m}^{-2}$  over NEC,  $6.64 \text{ W m}^{-2}$  over SEC, and  $5.35 \text{ W m}^{-2}$   
465 over WC, Fig. 8a) indicates the warmer atmosphere induced by the increase in GHG  
466 concentrations via the Greenhouse Effect and related feedbacks. The downward surface  
467 clear sky LW radiation increases more over SEC due to more increase of water vapor  
468 in the atmosphere ( $2.08 \text{ kg m}^{-2}$  over SEC; Fig. 8b). The enhanced moisture transport  
469 from the South China Sea to SEC and moisture transport convergence (not shown) are  
470 responsible for moistening atmosphere over SEC. The enhanced moisture transport is  
471 induced by more water vapor evaporated from the warmer ocean and the southwesterly  
472 anomalies around the coast in SEC (Fig. 8d), which are related to the strengthened land-  
473 sea thermal contrast resulting from larger warming over land than over ocean (Fig. 8c).  
474 The enhanced moisture transport convergence over SEC is attributed to the increased  
475 moisture static energy related to more water vapor transport and the enhanced Western  
476 North Pacific Subtropical High (Fig. 8d) induced by the strengthened local Hadley  
477 circulation resulting from the increased tropical sea surface temperatures in response to  
478 GHG changes (Tian et al. 2018). These circulation and sea surface temperature  
479 responses are consistent with the previous studies (Lau and Kim 2017; Lau et al. 2017).  
480 The increase of net surface SW radiation is significant over NEC and WC ( $0.91 \text{ W m}^{-2}$   
481 over NEC and  $2.06 \text{ W m}^{-2}$  over WC; Fig. 8e), which warms the land surface in situ.  
482 The positive anomalies of shortwave cloud radiative effect (SW CRE;  $1.77 \text{ W m}^{-2}$  over



483 NEC and  $1.75 \text{ W m}^{-2}$  over WC; Fig. 8f) associated with the reduction of cloud cover  
484 over NEC and WC (Fig. 8g) result in the increased surface SW radiation. The reduction  
485 of cloud cover over NEC and WC is associated with large decrease in relative humidity  
486 (Fig. 8h) since the water vapor in the atmosphere over land is mainly controlled by  
487 transport from ocean and constrained by ocean warming and increases less than  
488 saturation specific humidity following the Clausius-Clapeyron relationship because  
489 stronger warming over land than over ocean (e.g., Dong et al. 2009; Boé and Terray  
490 2014). In summary, the seasonal mean land surface and therefore surface air  
491 temperature ( $T_{\text{max}}$  and  $T_{\text{min}}$ ) during extended summer increases directly by the  
492 strengthened Greenhouse Effect over whole China and indirectly by the positive LW  
493 feedback related to the increase in water vapor over SEC associated with circulation  
494 changes in response to GHG changes and by the positive SW feedback corresponding  
495 to the decrease in cloud cover over WC and NEC in which GHG change induced  
496 warming in sea surface temperature plays an important role for the water vapor and  
497 circulation changes. As a result, all the frequency, intensity, and spatial extent of these  
498 three types of HWs are increased. Particularly, the positive LW feedback over SEC  
499 plays an important role in the increase in frequency of compound and nighttime HWs,  
500 while the positive SW feedback over WC and NEC dominates the increase in frequency  
501 of daytime HWs and the increase in intensity of all three types of HWs.

## 502 **5.2 Induced by AA forcing**

503 The spatial patterns of summer mean changes of some key variables in response to  
504 AA changes are illustrated in Figure 9. The total aerosol optical depth (AOD) increases

505 over most part of China (Fig. 9a), resulting in the reduction of the surface clear sky SW  
506 radiation ( $-2.97 \text{ W m}^{-2}$  over China; Fig. 9b) through aerosol-radiation interaction, then  
507 leading to surface cooling. Especially, the surface air temperature over SEC ( $-0.28 \text{ }^\circ\text{C}$ ;  
508 Fig. 9h) decreases greatly due to much larger decrease in surface SW radiation ( $-6.37$   
509  $\text{ W m}^{-2}$  over SEC; Fig. 9c). However, although the AOD increases over NEC around  
510  $40^\circ\text{N}$ , the surface SW radiation does not decrease much, because significant positive  
511 changes of SW CRE over NEC ( $1.42 \text{ W m}^{-2}$  over NEC; Fig. 9d) contributed to by the  
512 decrease in cloud cover (Fig. 9e) offset the decrease in surface clear sky SW (Fig. 9b)  
513 and warm the surface air (Fig. 9h). The decrease in cloud cover is associated with the  
514 decrease in rainfall over NEC (Fig. 9f), which is featured by weakened EASM induced  
515 by decreased land-sea thermal contrast and weakened atmospheric stability (Tian et al.  
516 2018). In addition, Zhang et al. (2017) addressed that the increase in AA emission  
517 induces the increase in the frequency of summer drought over North China by using the  
518 Coupled Model Intercomparison Project Phase 5 (CMIP5) model simulations.  
519 Furthermore, the reduced precipitation over NEC leads to decrease in soil moisture (Fig.  
520 9g) and decrease in evaporation (not shown), reducing the upward latent heat fluxes  
521 (not shown). This increased SW radiation due to decreased cloud cover and reduced the  
522 upward latent heat fluxes due to decreased soil moisture and evaporation exert a  
523 positive feedback to warm the surface and therefore surface air (Fig. 9h). Therefore, it  
524 is the decrease in surface clear sky SW radiation related to the increase of AOD (Fig.  
525 9a and b) that induces the decreases in frequency and intensity of daytime HWs over  
526 SEC through aerosol-radiation interaction. On the other hand, it is the increased SW

527 CRE over NEC (Fig. 9d) related to weakened EASM overwhelming the decrease in  
528 clear sky SW radiation (Fig. 9b) and the local precipitation-soil moisture-temperature  
529 interactions that jointly cause the increases in the frequency and intensity of daytime  
530 HWs over NEC.

## 531 **6. Conclusions**

532 The decadal changes across the mid-1990s of three types of HWs, i.e. compound  
533 HWs, daytime HWs, and nighttime HWs, during extended summer (May–September)  
534 are detected on the aspects of frequency, intensity, and spatial extent by using the  
535 Chinese station dataset. A set of numerical time-sliced experiments is performed by an  
536 atmosphere-ocean-mixed-layer coupled model to assess the role of anthropogenic  
537 forcings, including changes in GHG concentrations and AA emissions, in generating  
538 the decadal changes of the three types of HWs, and to evaluate the different  
539 contributions of individual GHG forcing and individual AA forcing to the HW decadal  
540 changes and to understand physical processes involved. The principle results are  
541 concluded as follow.

542 The three types of HWs over China experienced significant rapid decadal changes  
543 across the mid-1990s, featured by the increase in frequency, the enhancement in  
544 intensity, and the expansion in spatial extent. The compound HWs change most  
545 remarkably in all three aspects. The changes of daytime and nighttime HWs are also  
546 significant, though not as dramatic as changes of the compound HWs.

547 Results of the model simulations demonstrate that the anthropogenic forcing,

548 including changes in GHG concentrations and AA emissions, has played a predominant  
549 role in generating the observed decadal changes in the frequency, intensity and spatial  
550 extent of the three types of HWs. The spatial patterns of changes of the three types of  
551 HWs are well reproduced by the atmosphere-ocean-mixed-layer coupled model  
552 MetUM-GOML1 in response to changes in GHG and AA forcings together (ALL  
553 forcing). Quantitatively, simulated changes in frequency and intensity over China and  
554 over three sub-regions in response to ALL forcing are also comparable to the observed  
555 changes.

556 Individually, GHG changes dominantly result in the simulated changes of the three  
557 types of HWs in response to ALL forcing, while AA changes make a relatively weak  
558 contribution, and the changes in GHG and AA forcing have distinct impacts on the  
559 changes of the three types of HWs. Changes in GHG concentrations play a crucial role  
560 in increasing the frequency, intensity, and spatial extent of all three types of HWs over  
561 China. Changes in AA emissions have a weak influence on compound and nighttime  
562 HWs. However, AA changes significantly increase the frequency and intensity of  
563 daytime HWs over NEC and decrease them over SEC.

564 The GHG changes increase the frequency, intensity, and spatial extent of the three  
565 types of HWs both directly via the strengthened Greenhouse Effect and indirectly via  
566 atmosphere and circulation feedbacks in which GHG change induced warming in sea  
567 surface temperature plays an important role. Over the sub-regions of WC and NEC,  
568 warmer atmosphere due to the increase in GHG concentrations, accompanied with  
569 limited increase in water vapor in the atmosphere, results in the reduction of cloud cover.

570 Increased surface downward SW radiation, resulted from positive SW cloud radiative  
571 effect over WC and NEC, heats the surface and warms the surface air as a positive  
572 feedback. Over the sub-region of SEC, the increase of water vapor in the atmosphere,  
573 induced by the enhanced moisture transport and moisture transport convergence over  
574 SEC due to the circulation changes and warming in sea surface temperature in response  
575 to GHG changes, has a positive feedback on surface warming.

576 The AA changes significantly decrease the frequency and intensity of daytime HWs  
577 over SEC through aerosol-radiation interaction and increase them over NEC by the AA  
578 change induced rainfall change and atmosphere-surface feedbacks related to weakened  
579 East Asian summer monsoon. Increased AOD over eastern part of China directly  
580 reduces the surface SW radiation and decreases the surface temperature and surface air  
581 temperature over SEC and therefore the frequency and intensity of daytime HWs.  
582 Reduced cloud cover over NEC, resulting from the decrease in convection in response  
583 to AA changes, increases the surface SW radiation and warms the surface and surface  
584 air. The reduced rainfall also leads to decreased upward latent heat fluxes due to  
585 decreased soil moisture, which cooperated with the increased SW radiation related to  
586 less cloud cover tends to warm the surface. These surface feedbacks overwhelm the  
587 direct cooling impact induced by increase in AA emissions and lead to increases in the  
588 frequency and intensity of daytime HWs over NEC.

589 The results demonstrate the dominant contributions of anthropogenic changes,  
590 especially the increased GHG concentrations, to the observed decadal changes in  
591 frequency, intensity, and spatial extent of the three types of HWs over China during

592 extended summer across the mid-1990s. The GHG changes raise the mean surface air  
593 temperature and air column temperature, increasing all the aspects of the three types of  
594 HWs nearly over whole China with important water vapor feedbacks associated with  
595 GHG induced sea surface temperature changes. The AA changes have different local  
596 impacts. Local interaction between reduced precipitation, cloud cover, soil moisture,  
597 evaporation, and temperature related to weakened East Asian summer monsoon play  
598 an important role in warming the surface atmosphere over NEC and therefore changing  
599 the properties of daytime HWs.

600 Looking for a few decades ahead, GHGs will continue to increase while aerosol  
601 emissions over China are expecting to decrease. China would experience more HWs  
602 for different types over different regions with greater severity and the areas affected by  
603 severe HWs would also be expanded. Therefore, better strategies for adaptation and  
604 mitigation against different types of HWs over different regions would benefit the  
605 people and society.

606 This paper primarily investigates the individual roles of GHG concentrations and AA  
607 emissions in the decadal change of the three types of HWs over China. There are some  
608 other factors that could affect the decadal change of HWs over China, such as the land  
609 use and land cover change (Findell et al. 2017, Li et al. 2018a) and the phase shift of  
610 Atlantic Multi-decadal Oscillation, which might have contributed to warming over the  
611 Eurasian continent around mid-1990s (Hong et al. 2017). More effort is needed to  
612 quantify their contributions to the recent decadal changes of HWs over China.

613 Moreover, the responses to AA forcing are influenced not only by the AA emissions,  
614 but also by climatology, aerosol transport and deposition, and chemical processes in the  
615 model. All these processes affect the distribution of aerosol burden (e.g., Wilcox et al.  
616 2015b) and suggest a possible model dependence of the responses to AA forcing.  
617 Wang et al. (2018) pointed out that there are large intermodel spread of responses to  
618 AA forcings in different climate models. These model dependence and intermodel  
619 uncertainty of the responses call for improved model to investigate the responses to AA  
620 forcings.

621

## 622 **Acknowledgement**

623 This study is supported by the National Natural Science Foundation of China under  
624 Grants 41505037, U1502233, by the Applied Basic Research Foundation of Yunnan  
625 Province (2016FB078), and by the UK-China Research & Innovation Partnership Fund  
626 through the Met Office Climate Science for Service Partnership (CSSP) China as part  
627 of the Newton Fund. QS is supported by China Scholarship Council. BD is supported  
628 by the U.K. National Centre for Atmospheric Science-Climate (NCAS-Climate) at the  
629 University of Reading. The authors like to thank three anonymous reviewers for their  
630 constructive comments on the earlier version of the paper.

631

632

633

634

635

636

637

638

639

640

641

642

643

644

645 **References**

646 Alexander, L. V., X. Zhang, T. C. Peterson, J. Caesar, B. Gleason, A. M. G. K. Tank, M.

647 Haylock, D. Collins, B. Trewin and F. Rahimzadeh, 2006: Global observed

648 changes in daily climate extremes of temperature and precipitation. *J. Geophys.*

649 *Res. Atmos.*, **111**(D5), 1042-1063, <https://doi.org/10.1029/2005JD00629>.

650 Argueso, D., A. Di Luca, S. Perkins-Kirkpatrick, and J. P. Evans, 2016: Seasonal mean

651 temperature changes control future heat waves, *Geophys. Res. Lett.*, **43**, 7653–

652 7660, <https://doi.org/10.1002/2016GL069408>.



653 Arribas, A., M. Glover, A. Maidens, K. Peterson, M. Gordon, C. MacLachlan, R.  
654 Graham, D. Fereday, J. Camp and A. Scaife, 2011: The GloSea4 ensemble  
655 prediction system for seasonal forecasting. *Mon. Wea. Rev.*, **139**(6), 1891-1910,  
656 <https://doi.org/10.1175/2010MWR3615.1>.

657 Boé, J. and L. Terray, 2014: Land–sea contrast, soil-atmosphere and cloud-temperature  
658 interactions: interplays and roles in future summer European climate change.  
659 *Climate Dyn.*, **42**(3-4), 683-699, <https://doi.org/10.1007/s00382-013-1868-8>.

660 Chen, W. and B. Dong, 2018: Anthropogenic impacts on recent decadal change in  
661 temperature extremes over China: relative roles of greenhouse gases and  
662 anthropogenic aerosols. *Climate Dyn.*, [https://doi.org/10.1007/s00382-018-4342-](https://doi.org/10.1007/s00382-018-4342-9)  
663 9.

664 Chen, Y. and P. Zhai, 2017: Revisiting summertime hot extremes in China during  
665 1961- 2015: overlooked compound extremes and significant changes. *Geophys.*  
666 *Res. Lett.*, **44**(10), <https://doi.org/10.1002/2016GL072281>.

667 Chen, Y. and Y. Li, 2017: An Inter-comparison of Three Heat Wave Types in China  
668 during 1961-2010: Observed Basic Features and Linear Trends. *Sci. Rep.*, **7**, 45619,  
669 <https://doi.org/10.1038/srep45619>.

670 Coumou, D. and S. Rahmstorf, 2012: A decade of weather extremes. *Nat. Climate*  
671 *Change*, **2**(7), 491-496, <https://doi.org/10.1038/nclimate1452>.

672 Cubasch, U., G. A. Meehl, G. J. Boer, R. J. Stouffer, M. Dix, A. Noda, C. A. Senior, S.  
673 Raper and K. S. Yap, 2001: Projections of future climate change. *The Scientific*  
674 *Basis: Contribution of Working Group I to the Third Assessment Report of the*

675 *Intergovernmental Panel*, 526-582.

676 Della-Marta, P. M., J. Luterbacher, H. von Weissenfluh, E. Xoplaki, M. Brunet and H.  
677 Wanner, 2007: Summer heat waves over western Europe 1880–2003, their  
678 relationship to large-scale forcings and predictability. *Climate Dyn.*, **29**(2), 251-  
679 275, <https://doi.org/10.1007/s00382-007-0233-1>.

680 Ding, T., W. H. Qian and Z. W. Yan, 2010: Changes in hot days and heat waves in China  
681 during 1961-2007. *Int. J. Climatol.*, **30**(10), 1452-1462,  
682 <https://doi.org/10.1002/joc.1989>.

683 Donat, M. G., L. V. Alexander, H. Yang, I. Durre, R. Vose, R. J. H. Dunn, K. M. Willett,  
684 E. Aguilar, M. Brunet and J. Caesar, 2013: Updated analyses of temperature and  
685 precipitation extreme indices since the beginning of the twentieth century: The  
686 HadEX2 dataset. *J. Geophys. Res. Atmos.*, **118**(5), 2098-2118,  
687 <https://doi.org/10.1002/jgrd.50150>

688 Dong, B., J. M. Gregory and R. T. Sutton, 2009: Understanding land–sea warming  
689 contrast in response to increasing greenhouse gases. Part I: Transient adjustment.  
690 *J. Climate*, **22**(11), 3079-3097, <https://doi.org/10.1175/2009JCLI2652.1>.

691 Dong, B., R. T. Sutton, E. J. Highwood and L. J. Wilcox, 2016a: Preferred response of  
692 the East Asian summer monsoon to local and non-local anthropogenic sulphur  
693 dioxide emissions. *Climate Dyn.*, **46**(5), 1733-1751,  
694 <https://doi.org/10.1007/s00382-015-2671-5>.

695 Dong, B., R. T. Sutton, L. Shaffrey and N. P. Klingaman, 2017: Attribution of Forced  
696 Decadal Climate Change in Coupled and Uncoupled Ocean–Atmosphere Model

697 Experiments. *J. Climate*, **30**(16), 6203-6223, <https://doi.org/10.1175/jcli-d-16->  
698 0578.1.

699 Dong, B., R. T. Sutton, W. Chen, X. Liu, R. Lu and Y. Sun, 2016b: Abrupt summer  
700 warming and changes in temperature extremes over Northeast Asia since the mid-  
701 1990s: drivers and physical processes. *Adv. Atmos. Sci.*, **33**(9), 1005-1023,  
702 <https://doi.org/10.1007/s00376-016-5247-3>.

703 Feichter, J., E. Roeckner, U. Lohmann and B. Liepert, 2004: Nonlinear aspects of the  
704 climate response to greenhouse gas and aerosol forcing. *J. Climate*, **17**(12), 2384-  
705 2398, [https://doi.org/10.1175/1520-0442\(2004\)017<2384:naotcr>2.0.co;2](https://doi.org/10.1175/1520-0442(2004)017<2384:naotcr>2.0.co;2).

706 Findell, K. L., Berg, A., Gentine, P., Krasting, J. P., Lintner, B. R., Malyshev, S., et al.  
707 2017: The impact of anthropogenic land use and land cover change on regional  
708 climate extremes. *Nature Communications*, **8**(1), 989.  
709 <https://doi.org/10.1038/s41467-017-01038-w>.

710 Fischer, E. M., S. I. Seneviratne, P. L. Vidale, D. Lüthi and C. Schär, 2007: Soil  
711 moisture–atmosphere interactions during the 2003 European summer heat wave.  
712 *J. Climate*, **20**(20), 5081-5099, <https://doi.org/10.1175/JCLI4288.1>.

713 Freychet, N., S. Tett, J. Wang and G. Hegerl, 2017: Summer heat waves over Eastern  
714 China: dynamical processes and trend attribution. *Environ. Res. Lett.*, **12**(2),  
715 024015, <https://doi.org/10.1088/1748-9326/aa5ba3>.

716 Freychet, N., S. Tett, G. Hegerl, and J. Wang, 2018a: Central-Eastern China persistent  
717 heat waves: Evaluation of the AMIP models. *J. Climate*, **31**(9), 3609-3624,  
718 <https://doi.org/10.1175/JCLI-D-17-0480.1>

719 Freychet, N., S. Sparrow, S. F. B. Tett, M. J. Mineter, G. C. Hegerl and D. C. H. Wallom,  
720 2018b: Impacts of Anthropogenic Forcings and El Nino on Chinese Extreme  
721 Temperatures. *Adv. Atmos. Sci.*, **35**(8), 994-1002, [https://doi.org/10.1007/s00376-](https://doi.org/10.1007/s00376-018-7258-8)  
722 018-7258-8.

723 Gosling, S. N., J. A. Lowe, G. R. McGregor, M. Pelling and B. D. Malamud, 2009:  
724 Associations between elevated atmospheric temperature and human mortality: a  
725 critical review of the literature. *Climatic change*, **92**(3-4), 299-341,  
726 <https://doi.org/10.1007/s10584-008-9441-x>.

727 Guo, L., Highwood, E. J., Shaffrey, L. C. and Turner, A. G., 2013: The effect of regional  
728 changes in anthropogenic aerosols on rainfall of the East Asian Summer Monsoon.  
729 *Atmos. Chem. and Phys.*, **13**(3), 1521 – 1534. [https://doi.org/10.5194/acp-13-1521-](https://doi.org/10.5194/acp-13-1521-2013)  
730 2013.

731 Guo, X., J. Huang, Y. Luo, Z. Zhao and Y. Xu, 2017: Projection of heat waves over  
732 China for eight different global warming targets using 12 CMIP5 models. *Theor.*  
733 *Appl. Climatol.*, **128**(3-4), 507-522, <https://doi.org/10.1007/s00704-015-1718-1>.

734 Hajat, S., B. Armstrong, M. Baccini, A. Biggeri, L. Bisanti, A. Russo, A. Paldy, B.  
735 Menne and T. Kosatsky, 2006: Impact of high temperatures on mortality: is there  
736 an added heat wave effect? *Epidemiology*, **17**(6), 632-638,  
737 <https://doi.org/10.1097/01.ede.0000239688.70829.63>.

738 Hirons, L., N. Klingaman and S. Woolnough, 2015: MetUM-GOML: a near-globally  
739 coupled atmosphere–ocean-mixed-layer model. *Geosci. Model Dev.*, **8**, 363-379,  
740 <https://doi.org/10.5194/gmd-8-363-2015>.

741 Hong, J. S., S. W. Yeh and K. H. Seo, 2018: Diagnosing physical mechanisms leading  
742 to pure heat waves versus pure tropical nights over the Korean Peninsula. *J.*  
743 *Geophys. Res. Atmos.*, **123**(14), 7149-7160, <https://doi.org/10.1029/2018jd028360>.

744 Hong, X., R. Lu and S. Li, 2017: Amplified summer warming in Europe-West Asia and  
745 Northeast Asia after the mid-1990s. *Environ. Res. Lett.*

746 Jones, P. D., S. C. B. Raper, R. S. Bradley, H. F. Diaz, P. M. Kelly and T. M. L. Wigley,  
747 1986: Northern hemisphere surface air temperature variations: 1851-1984.  
748 *Journal of Climate and Applied Meteorology*, **25**(2), 161-179,  
749 [https://doi.org/10.1175/1520-0450\(1986\)025<0161:nhsatv>2.0.co;2](https://doi.org/10.1175/1520-0450(1986)025<0161:nhsatv>2.0.co;2).

750 Lamarque, J.-F., G. P. Kyle, M. Meinshausen, K. Riahi, S. J. Smith, D. P. van Vuuren,  
751 A. J. Conley and F. Vitt, 2011: Global and regional evolution of short-lived  
752 radiatively-active gases and aerosols in the Representative Concentration  
753 Pathways. *Climatic change*, **109**, 191, <https://doi.org/10.1007/s10584-011-0155-0>.

754 Lamarque, J.-F., T. C. Bond, V. Eyring, C. Granier, A. Heil, Z. Klimont, D. Lee, C.  
755 Liousse, A. Mieville and B. Owen, 2010: Historical (1850–2000) gridded  
756 anthropogenic and biomass burning emissions of reactive gases and aerosols:  
757 methodology and application. *Atmos. Chem. Phys.*, **10**(15), 7017-7039,  
758 <https://doi.org/10.5194/acp-10-7017-2010>.

759 Le Quéré, C., M. R. Raupach, J. G. Canadell, G. Marland, L. Bopp, P. Ciais, T. J.  
760 Conway, S. C. Doney, R. A. Feely, P. Foster, P. Friedlingstein, K. Gurney, R. A.  
761 Houghton, J. I. House, C. Huntingford, P. E. Levy, M. R. Lomas, J. Majkut, N.  
762 Metzl, J. P. Ometto, G. P. Peters, I. C. Prentice, J. T. Randerson, S. W. Running, J.

763 L. Sarmiento, U. Schuster, S. Sitch, T. Takahashi, N. Viovy, G. R. van der Werf  
764 and F. I. Woodward, 2009: Trends in the sources and sinks of carbon dioxide. *Nat.*  
765 *Geosci.*, 2, 831, <https://doi.org/10.1038/ngeo689>.

766 Lau, W. K. M., K. M. Kim and L. R. Leung, 2017: Changing circulation structure and  
767 precipitation characteristics in Asian monsoon regions: greenhouse warming vs.  
768 aerosol effects. *Geosci. Lett.*, 4(1), 28, [https://doi.org/10.1186/s40562-017-0094-](https://doi.org/10.1186/s40562-017-0094-3)  
769 3.

770 Lau, W. K. M. and K. M. Kim, 2017: Competing influences of greenhouse warming  
771 and aerosols on Asian summer monsoon circulation and rainfall. *Asia-Pac. J. Atmo.*  
772 *Sci.*, 53(2), 181-194, <https://doi.org/10.1007/s13143-017-0033-4>.

773 Li, X., Chen, H., Wei, J., Hua, W., Sun, S., Ma, H., et al., 2018a: Inconsistent responses  
774 of hot extremes to historical land use and cover change among the selected CMIP5  
775 models. *J. Geophys. Res. Atmos.*, 123, 3497–3512,  
776 <https://doi.org/10.1002/2017JD028161>

777 Li, X. and M. Ting, 2017: Understanding the Asian summer monsoon response to  
778 greenhouse warming: the relative roles of direct radiative forcing and sea surface  
779 temperature change. *Climate Dyn.*, 49(7-8), 2863-2880,  
780 <https://doi.org/10.1007/s00382-016-3470-3>.

781 Li, X., M. Ting and D. E. Lee, 2018b: Fast Adjustments of the Asian Summer Monsoon  
782 to Anthropogenic Aerosols. *Geophys. Res. Lett.*, 45(2), 1001-1010,  
783 <https://doi.org/10.1002/2017gl076667>.

784 Li, Y., Y. Ding and W. Li, 2017: Observed Trends in Various Aspects of Compound

785 Heat Waves across China from 1961 to 2015. *J. Meteor. Res.*, **31**(3), 455-467,  
786 <https://doi.org/10.1007/s13351-017-6150-2>.

787 Li, Z., L. J. Cao, Y. N. Zhu and Z. W. Yan, 2016a: Comparison of Two Homogenized  
788 Datasets of Daily Maximum/Mean/Minimum Temperature in China during 1960-  
789 2013. *J. Meteor. Res.*, **30**(1), 53-66, <https://doi.org/10.1007/s13351-016-5054-x>.

790 Li, Z., W. K. M. Lau, V. Ramanathan, G. Wu, Y. Ding, M. G. Manoj, et al., 2016b:  
791 Aerosol and monsoon climate interactions over Asia. *Rev. Geophys.*, **54**(4), 866-  
792 929, <https://doi.org/10.1002/2015rg000500>.

793 Lu, C. H., Y. Sun, H. Wan, X. B. Zhang and H. Yin, 2016: Anthropogenic influence on  
794 the frequency of extreme temperatures in China. *Geophys. Res. Lett.*, **43**(12),  
795 6511-6518, <https://doi.org/10.1002/2016gl069296>.

796 Lu, R. Y. and R. D. Chen, 2016: A review of recent studies on extreme heat in China.  
797 *Atmos. Oceanic Sci. Lett.*, **9**(2), 114-121,  
798 <https://doi.org/10.1080/16742834.2016.1133071>.

799 Luo, M. and N.-C. Lau, 2017: Heat waves in southern China: Synoptic behavior, long-  
800 term change, and urbanization effects. *J. Climate*, **30**(2), 703-720,  
801 <https://doi.org/10.1175/jcli-d-16-0269.1>.

802 Luo, F., B. Dong, F. Tian and S. Li, 2018: Anthropogenically forced decadal change of  
803 South Asian summer monsoon across the mid-1990s. Submitted to *Journal of*  
804 *Geophys. Res. Atmos.*

805 Ma, S. M., T. J. Zhou, D. A. Stone, O. Angelil and H. Shiogama, 2017: Attribution of  
806 the July-August 2013 heat event in Central and Eastern China to anthropogenic

807 greenhouse gas emissions. *Environ. Res. Lett.*, **12**(5),  
808 <https://doi.org/10.1088/1748-9326/aa69d2>.

809 Matsueda, M., 2011: Predictability of Euro- Russian blocking in summer of 2010.  
810 *Geophys. Res. Lett.*, **38**(6), <https://doi.org/10.1029/2010GL046557>

811 Meehl, G. A. and C. Tebaldi, 2004: More intense, more frequent, and longer lasting  
812 heat waves in the 21st Century. *Science*, **305**(5686), 994-997,  
813 <https://doi.org/10.1126/science.1098704>.

814 Ming, Y. and V. Ramaswamy, 2009: Nonlinear climate and hydrological responses to  
815 aerosol effects. *J. Climate*, **22**(6), 1329-1339,  
816 <https://doi.org/10.1175/2008jcli2362.1>.

817 Perkins, S. E., 2015: A review on the scientific understanding of heatwaves—Their  
818 measurement, driving mechanisms, and changes at the global scale. *Atmos. Res.*,  
819 **164–165**, 242-267, <https://doi.org/10.1016/j.atmosres.2015.05.014>.

820 Perkins, S. E. and L. V. Alexander, 2013: On the Measurement of Heat Waves. *J.*  
821 *Climate*, **26**(13), 4500-4517, <https://doi.org/10.1175/jcli-d-12-00383.1>.

822 Rayner, N. A., D. E. Parker, E. B. Horton, C. K. Folland, L. V. Alexander, D. P. Rowell,  
823 E. C. Kent and A. Kaplan, 2003: Global analyses of sea surface temperature, sea  
824 ice, and night marine air temperature since the late nineteenth century. *J. Geophys.*  
825 *Res. Atmos.*, **108**(D14), <https://doi.org/10.1029/2002JD002670>.

826 Robine, J.-M., S. L. K. Cheung, S. Le Roy, H. Van Oyen, C. Griffiths, J.-P. Michel and  
827 F. R. Herrmann, 2008: Death toll exceeded 70,000 in Europe during the summer  
828 of 2003. *C. R. Biol.*, **331**(2), 171-178, <https://doi.org/10.1016/j.crvi.2007.12.001>.



829 Rosenfeld, D., U. Lohmann, G. B. Raga, C. D. O'Dowd, M. Kulmala, S. Fuzzi, A.  
830 Reissell and M. O. Andreae, 2008: Flood or drought: how do aerosols affect  
831 precipitation? *Science*, **321**(5894), 1309-1313,  
832 <https://doi.org/10.1126/science.1160606>.

833 Schär, C. and G. Jendritzky, 2004: Climate change: hot news from summer 2003.  
834 *Nature*, **432**(7017), 559, <https://doi.org/10.1038/432559a>.

835 Seneviratne, S. I., M. G. Donat, B. Mueller and L. V. Alexander, 2014: No pause in the  
836 increase of hot temperature extremes. *Nat. Climate Change*, **4**(3), 161,  
837 <https://doi.org/10.1038/nclimate2145>.

838 Shiogama, H., D. A. Stone, T. Nagashima, T. Nozawa and S. Emori, 2013: On the linear  
839 additivity of climate forcing- response relationships at global and continental  
840 scales. *Int. J. Climatol.*, **33**(11), 2542-2550, <https://doi.org/10.1002/joc.3607>

841 Smith, D. M. and J. M. Murphy, 2007: An objective ocean temperature and salinity  
842 analysis using covariances from a global climate model. *J. Geophys. Res. Oceans*,  
843 **112**(C2), <https://doi.org/10.1029/2005JC003172>.

844 Stefanon, M., D. A. Fabio and D. Philippe, 2012: Heatwave classification over Europe  
845 and the Mediterranean region. *Environ. Res. Lett.*, **7**(1), 014023,  
846 <https://doi.org/10.1088/1748-9326/7/1/014023>.

847 Stevens, B. and G. Feingold, 2009: Untangling aerosol effects on clouds and  
848 precipitation in a buffered system. *Nature*, **461**(7264), 607,  
849 <https://doi.org/10.1038/nature08281>.

850 Sun, Y., L. Song, H. Yin, B. Zhou, T. Hu, X. Zhang and P. Stott, 2016: Human influence

851 on the 2015 extreme high temperature events in Western China [in "Explaining  
852 Extremes of 2015 from a Climate Perspective"]. *Bull. Amer. Meteor. Soc.*, **97**(12),  
853 S102-S106, <https://doi.org/10.1175/bams-d-16-0158.1>.

854 Sun, Y., X. B. Zhang, F. W. Zwiers, L. C. Song, H. Wan, T. Hu, H. Yin and G. Y. Ren,  
855 2014: Rapid increase in the risk to extreme summer heat in Eastern China. *Nat.*  
856 *Climate Change*, **4**(12), 1082-1085, <https://doi.org/10.1038/nclimate2410>.

857 Tan, J., Y. Zheng, G. Song, L. S. Kalkstein, A. J. Kalkstein and X. Tang, 2007: Heat  
858 wave impacts on mortality in Shanghai, 1998 and 2003. *Int. J. Biometeorol.*, **51**(3),  
859 193-200, <https://doi.org/10.1007/s00484-006-0058-3>.

860 Tao, W. K., J. P. Chen, Z. Li, C. Wang and C. Zhang, 2012: Impact of aerosols on  
861 convective clouds and precipitation. *Rev. Geophys.*, **50**(2), RG2001,  
862 <https://doi.org/10.1029/2011RG000369>.

863 Tian, F., B. Dong, J. Robson and R. Sutton, 2018: Forced decadal changes in the East  
864 Asian summer monsoon: the roles of greenhouse gases and anthropogenic aerosols.  
865 *Climate Dyn.*, 1-17, <https://doi.org/10.1007/s00382-018-4105-7>.

866 Walters, D., M. Best, A. Bushell, D. Copsey, J. Edwards, P. Falloon, C. Harris, A. Lock,  
867 J. Manners and C. Morcrette, 2011: The Met Office Unified Model global  
868 atmosphere 3.0/3.1 and JULES global land 3.0/3.1 configurations. *Geosci. Model*  
869 *Dev.*, **4**(4), 919, <https://doi.org/10.5194/gmd-4-919-2011>.

870 Wang, H., S. Xie, Y. Kosaka, Q. Liu, and Y. Du, 2018: Dynamics of Asian Summer  
871 Monsoon response to anthropogenic aerosol forcing. *J. Climate*.  
872 <https://doi.org/10.1175/JCLI-D-18-0386.1>

873 Wang, P., J. Tang, X. Sun, S. Wang, J. Wu, X. Dong and J. Fang, 2017: Heatwaves in  
874 China: definitions, leading patterns and connections to large-scale atmospheric  
875 circulation and SSTs. *J. Geophys. Res. Atmos.*, **122**(20),  
876 <https://doi.org/10.1002/2017JD027180>.

877 Wen, Q. Z. H., X. B. Zhang, Y. Xu and B. Wang, 2013: Detecting human influence on  
878 extreme temperatures in China. *Geophys. Res. Lett.*, **40**(6), 1171-1176,  
879 <https://doi.org/10.1002/grl.50285>.

880 Wilcox, L. J., B. Dong, R. T. Sutton and E. J. Highwood, 2015a: The 2014 hot, dry  
881 summer in Northeast Asia [in "Explaining Extremes of 2014 from a Climate  
882 Perspective"]. *Bull. Amer. Meteor. Soc.*, **96**(12), S105-S110,  
883 <https://doi.org/10.1175/bams-d-15-00123.1>.

884 Wilcox, L. J., E. J. Highwood, B. B. Booth, K. S. Carslaw, 2015b: Quantifying  
885 sources of inter-model diversity in the cloud albedo effect. *Geophys. Res. Lett.*, **42**,  
886 1568-1575. ISSN 0094-8276 doi: <https://doi.org/10.1002/2015GL063301>

887 Yin, H., Y. Sun, H. Wan, X. B. Zhang and C. H. Lu, 2017: Detection of anthropogenic  
888 influence on the intensity of extreme temperatures in China. *Int. J. Climatol.*, **37**(3),  
889 1229-1237, <https://doi.org/10.1002/joc.4771>.

890 You, Q. L., Z. H. Jiang, L. Kong, Z. W. Wu, Y. T. Bao, S. C. Kang and N. Pepin, 2017:  
891 A comparison of heat wave climatologies and trends in China based on multiple  
892 definitions. *Climate Dyn.*, **48**(11), 3975-3989, [https://doi.org/10.1007/s00382-](https://doi.org/10.1007/s00382-016-3315-0)  
893 [016-3315-0](https://doi.org/10.1007/s00382-016-3315-0).

894 Zhang, L. X., P. L. Wu and T. J. Zhou, 2017: Aerosol forcing of extreme summer

895 drought over North China. *Environ. Res. Lett.*, **12**(3),

896 <https://doi.org/10.1088/1748-9326/aa5fb3>.

897 Zhou, T. J., S. M. Ma and L. W. Zou, 2014: Understanding a hot summer in Central

898 Eastern China: summer 2013 in context of multimodel trend analysis [in

899 "Explaining Extremes of 2013 from a Climate Perspective"]. *Bull. Amer. Meteor.*

900 *Soc.*, **95**(9), S54-S57.

901

902

903

904

905

906

907

908

909

910

911

912

913

914

915 **Tables**

916 **Table 1.** Summary of numerical experiments: Note that a slightly different period of

917 1970-1981 for the aerosol forcing in the early period (EP) is used since aerosol  
 918 emissions data before 1970 were not available.

<b>Abv.</b>	<b>Experiment</b>	<b>Ocean</b>	<b>Radiative forcing</b>
<b>R0</b>	Relaxation run	Relaxation to “present day” (PD, 1994-2011) mean 3D ocean temperature and salinity to diagnose climatological temperature and salinity tendencies	PD greenhouse gases (GHGs) over 1994~2011 and anthropogenic aerosol (AA) emissions over 1994~2010 with AA after 2006 from RCP4.5 scenario (Lamarque et al. 2010, 2011)
<b>C-EP</b>	Early period (EP 1964~1981)		EP mean GHG and EP mean AA emissions
<b>C-PD</b>	Present Day (PD 1994~2011) with GHG and AA forcings	Climatological temperature and salinity tendencies from relaxation run	PD mean GHG and PD mean AA emissions
<b>C-PD-GHG</b>	Present Day (PD 1994~2011) with GHG forcing		PD mean GHG and EP mean AA emissions
<b>C-PD-AA</b>	Present Day (PD 1994~2011) with AA forcing		EP mean GHG and PD mean AA emissions

919

920 **Table 2.** Area averaged decadal changes of three type HW properties over China in  
 921 observations

	<b>Frequency</b> (events/ year)		<b>Intensity</b> (°C)		<b>Spatial extent</b> (10 <sup>6</sup> km <sup>2</sup> )	
	<b>EP</b>	<b>PD</b>	<b>EP</b>	<b>PD</b>	<b>EP</b>	<b>PD</b>
<b>Compound HWs</b>	0.67	1.85	1.42	3.09	3.66	6.97
<b>Dayti</b>	2.36	3.06	1.26	1.55	8.39	8.86

<b>me</b>						
<b>HWs</b>						
<b>Nightti</b>						
<b>me</b>	1.80	3.76	0.86	1.27	7.61	9.06
<b>HWs</b>						

922

923

924

925

926

927

928 **Figure captions**

929 **Figure 1.** Time series of area-averaged frequency (units: events/year; left panels), intensity  
930 (units: °C; middle panels), and spatial extent (units: 10<sup>6</sup> km<sup>2</sup>; right panels) of (a-c) compound, (d-f)  
931 daytime, and (g-i) nighttime HWs in extended summer over whole mainland of China (black solid  
932 lines), Northeastern China (blue dashed lines), Southeastern China (orange dashed lines), and  
933 Western China (green dashed lines). Black dashed lines denote the time means of area-averaged  
934 indicators. Red solid lines represent the decadal variations of area-averaged indicators, obtained by  
935 9-year running average. The black solid and dashed, as well as the red solid lines are for the left Y-  
936 axis, while the dashed blue, orange, and green lines are for the right Y-axis.

937 **Figure 2.** Spatial patterns of differences in frequency (units: events/year; left panels) and intensity  
938 (units: °C; right panels) of (a-b) compound, (c-d) daytime, and (e-f) nighttime HWs between the PD  
939 and EP. The slashes highlight the regions where the changes are statistically significant at the 90%  
940 confidence level based on a two-tailed Student *t*-test. (g) Distributions of 753 stations in China

941 station dataset. The three sub-regional groups are marked with different color dots. The dots in green,  
942 orange and purple represent the sub-regions of Northeastern China (NEC), Southeastern China (SEC)  
943 and Western China (WC), respectively.

944 **Figure 3.** Climatological means of extended-summer-mean (May–September) Tmax and Tmin  
945 during the PD (1994-2011) in observations (a and b) and in the C-PD experiment (c and d). Units  
946 are in °C.

947 **Figure 4.** Spatial patterns of changes in frequency (units: events/year; left panels) and intensity  
948 (units: °C; right panels) of compound HWs in response to changes in (a-b) ALL forcing, (c-d) GHG  
949 forcing, and (e-f) AA forcing, masked by China boundary. The slashes highlight the regions where  
950 the differences are statistically significant at the 90% confidence level based on a two-tailed Student  
951 *t*-test.

952 **Figure 5.** Spatial patterns of changes in frequency (units: events/year; left panels) and intensity  
953 (units: °C; right panels) of daytime HWs in response to changes in (a-b) ALL forcing, (c-d) GHG  
954 forcing, and (e-f) AA forcing, masked by China boundary. The slashes highlight the regions where  
955 the differences are statistically significant at the 90% confidence level based on a two-tailed Student  
956 *t*-test.

957 **Figure 6.** Spatial patterns of changes in frequency (units: events/year; left panels) and intensity  
958 (units: °C; right panels) of nighttime HWs in response to changes in (a-b) ALL forcing, (c-d) GHG  
959 forcing, and (e-f) AA forcing, masked by China boundary. The slashes highlight the regions where  
960 the differences are statistically significant at the 90% confidence level based on a two-tailed Student  
961 *t*-test.

962 **Figure 7.** Area averaged changes in frequency (units: events/year; left panels), intensity (units: °C;

963 middle panels), and spatial extent (units: km<sup>2</sup>; right panels) of (a-c) compound, (d-f) daytime, and  
964 (g-i) nighttime HWs over whole China, NEC, SEC, and WC in observations and simulations  
965 forced by ALL forcing, GHG forcing, and AA forcing. The error bars indicate the 90% confidence  
966 intervals based on two-tailed Student *t*-test.

967 **Figure 8.** Spatial patterns of extended-summer-mean response to changes in GHG forcing (C-PD-  
968 GHG minus C-EP): (a) surface clear sky downward LW radiation; (b) water vapor (units: kg m<sup>-2</sup>);  
969 (c) surface temperature (units: °C); (d) horizontal wind at 850 hPa (units: m s<sup>-1</sup>); (e) net surface SW  
970 radiation; (f) surface SW CRE; (g) total cloud cover (units: %) and (h) relative humidity at 700 hPa  
971 (units: %). Radiation with positive value meaning downward and in W m<sup>-2</sup>. The black dots in a-c  
972 and e-h and the blue shadings in d highlight regions where the changes are statistically significant  
973 at the 90% confidence level based on a two-tailed Student *t*-test.

974 **Figure 9.** Spatial patterns of extended-summer-mean response to changes in AA forcing (C-PD-AA  
975 minus C-EP): (a) total AOD at 0.55 um; (b) net clear sky surface SW radiation; (c) net surface SW  
976 radiation; (d) surface SW CRE; (e) total cloud cover (units: %); (f) precipitation (units: mm day<sup>-1</sup>);  
977 (g) soil moisture (units: kg m<sup>-2</sup>) and (h) Tmax (units: °C). Radiation with positive value meaning  
978 downward and in W m<sup>-2</sup>. The black dots highlight regions where the changes are statistically  
979 significant at the 90% confidence level based on a two-tailed Student *t*-test.

980

981

982

983

984



985

986

987

988

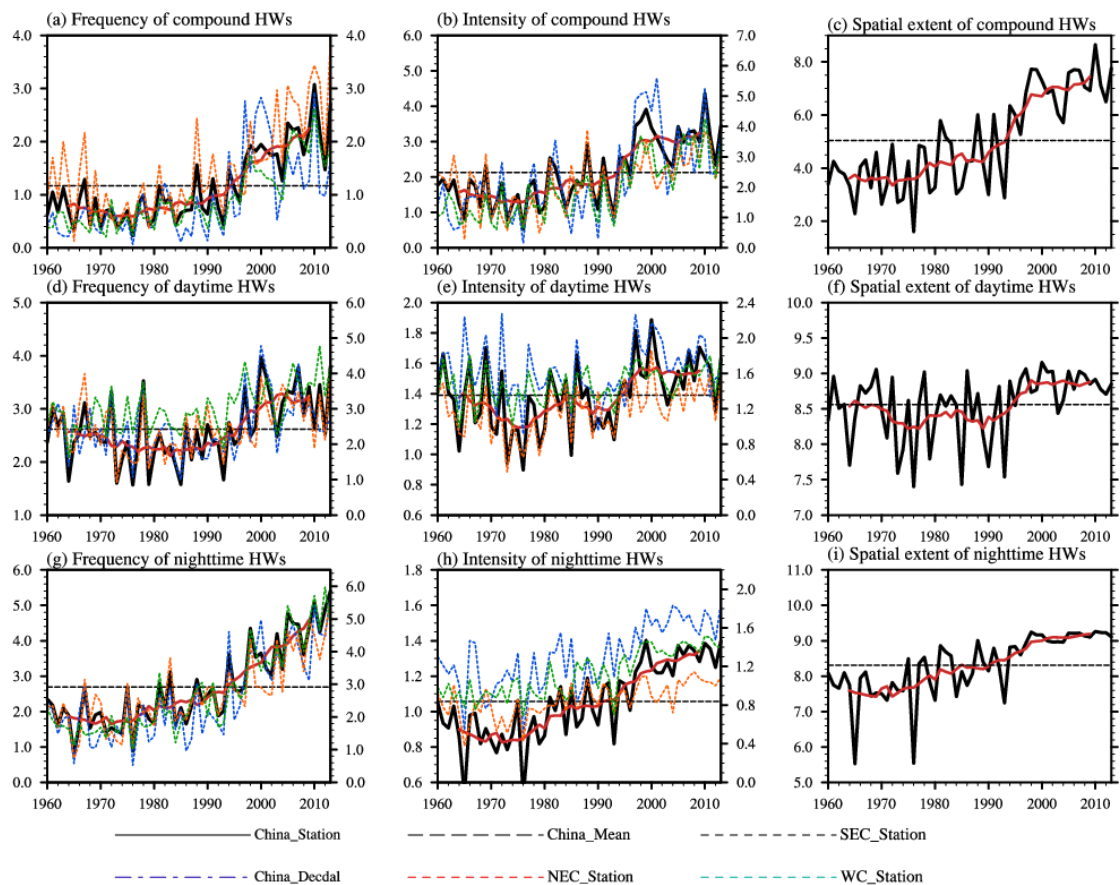
989

990

991

992

993 **Figures**



994

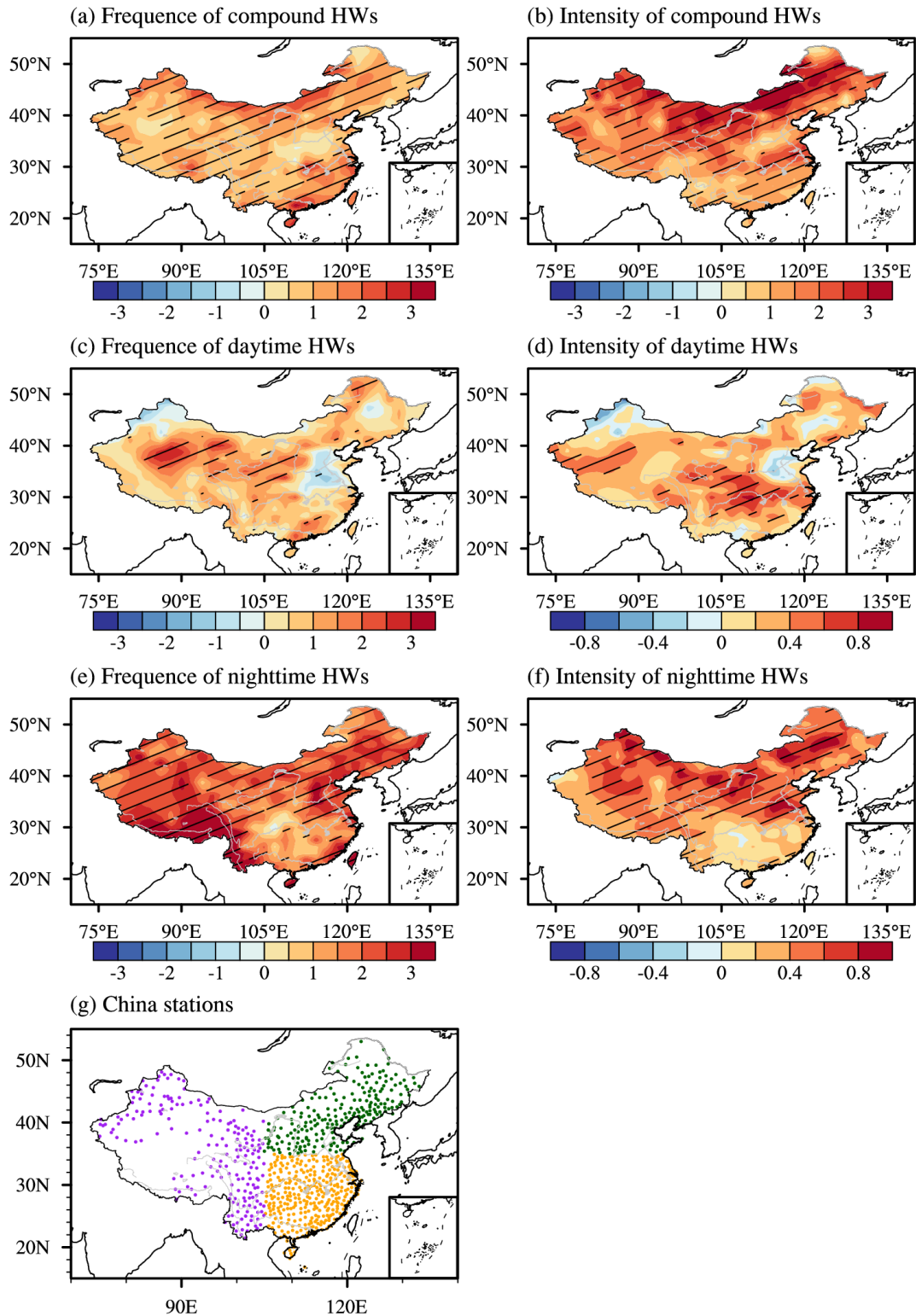
995 **Figure 1.** Time series of area-averaged frequency (units: events/year; left panels), intensity

996 (units: °C; middle panels), and spatial extent (units: 10<sup>6</sup> km<sup>2</sup>; right panels) of (a-c) compound, (d-f)

997 daytime, and (g-i) nighttime HWs in extended summer over whole mainland of China (black solid

998 lines), Northeastern China (blue dashed lines), Southeastern China (orange dashed lines), and  
999 Western China (green dashed lines). Black dashed lines denote the time means of area-averaged  
1000 indicators. Red solid lines represent the decadal variations of area-averaged indicators, obtained by  
1001 9-year running average. The black solid and dashed, as well as the red solid lines are for the left Y-  
1002 axis, while the dashed blue, orange, and green lines are for the right Y-axis.

1003



1004

1005 **Figure 2.** Spatial patterns of differences in frequency (units: events/year; left panels) and intensity

1006 (units: °C; right panels) of (a-b) compound, (c-d) daytime, and (e-f) nighttime HWs between the PD

1007 and EP. The slashes highlight the regions where the changes are statistically significant at the 90%

1008 confidence level based on a two-tailed Student *t*-test. (g) Distributions of 753 stations in China  
1009 station dataset. The three sub-regional groups are marked with different color dots. The dots in green,  
1010 orange and purple represent the sub-regions of Northeastern China (NEC), Southeastern China (SEC)  
1011 and Western China (WC), respectively.

1012

1013

1014

1015

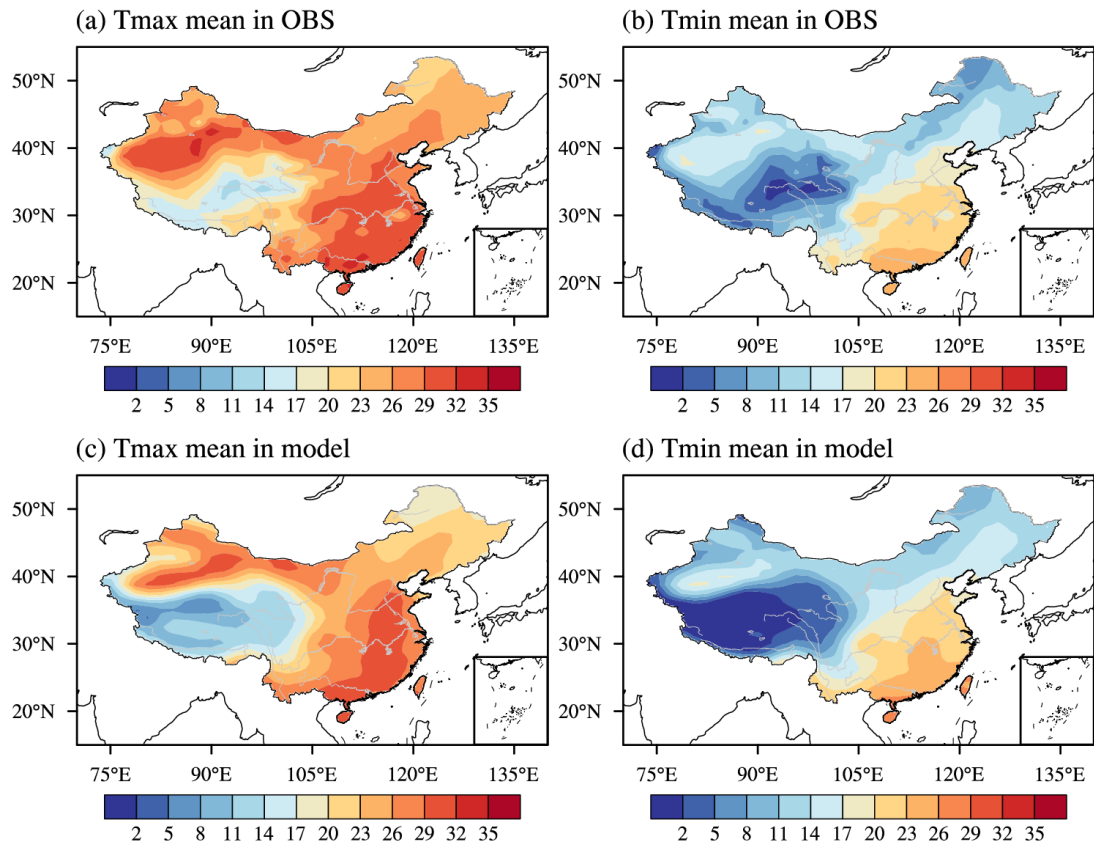
1016

1017

1018

1019

1020



1021

1022 **Figure 3.** Climatological means of extended-summer-mean (May–September) Tmax and Tmin

1023 during the PD (1994-2011) in observations (a and b) and in the C-PD experiment (c and d). Units

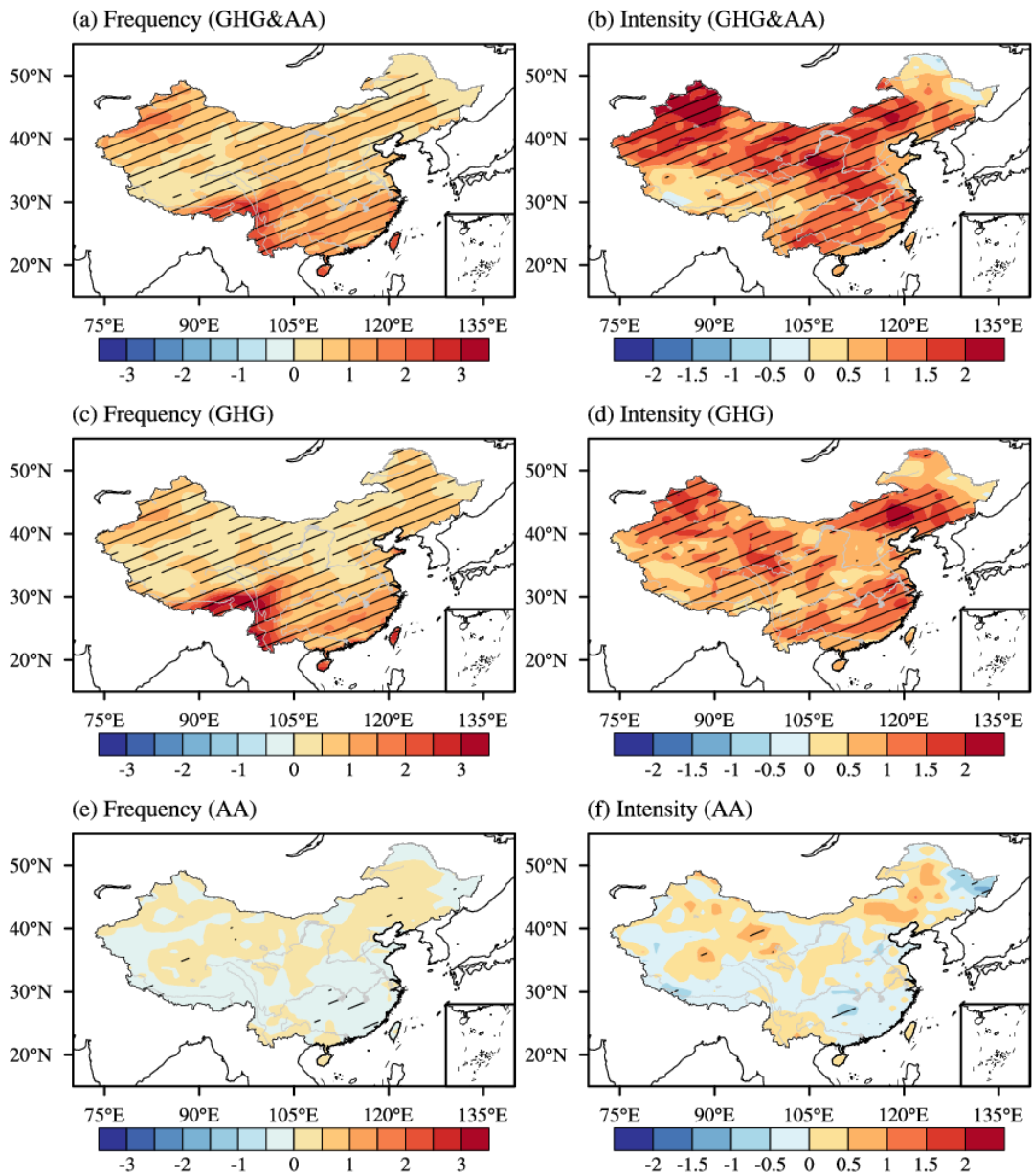
1024 are in °C

1025

1026

1027

1028



1029

1030 **Figure 4.** Spatial patterns of changes in frequency (units: events/year; left panels) and intensity

1031 (units: °C; right panels) of compound HWs in response to changes in (a-b) ALL forcing, (c-d) GHG

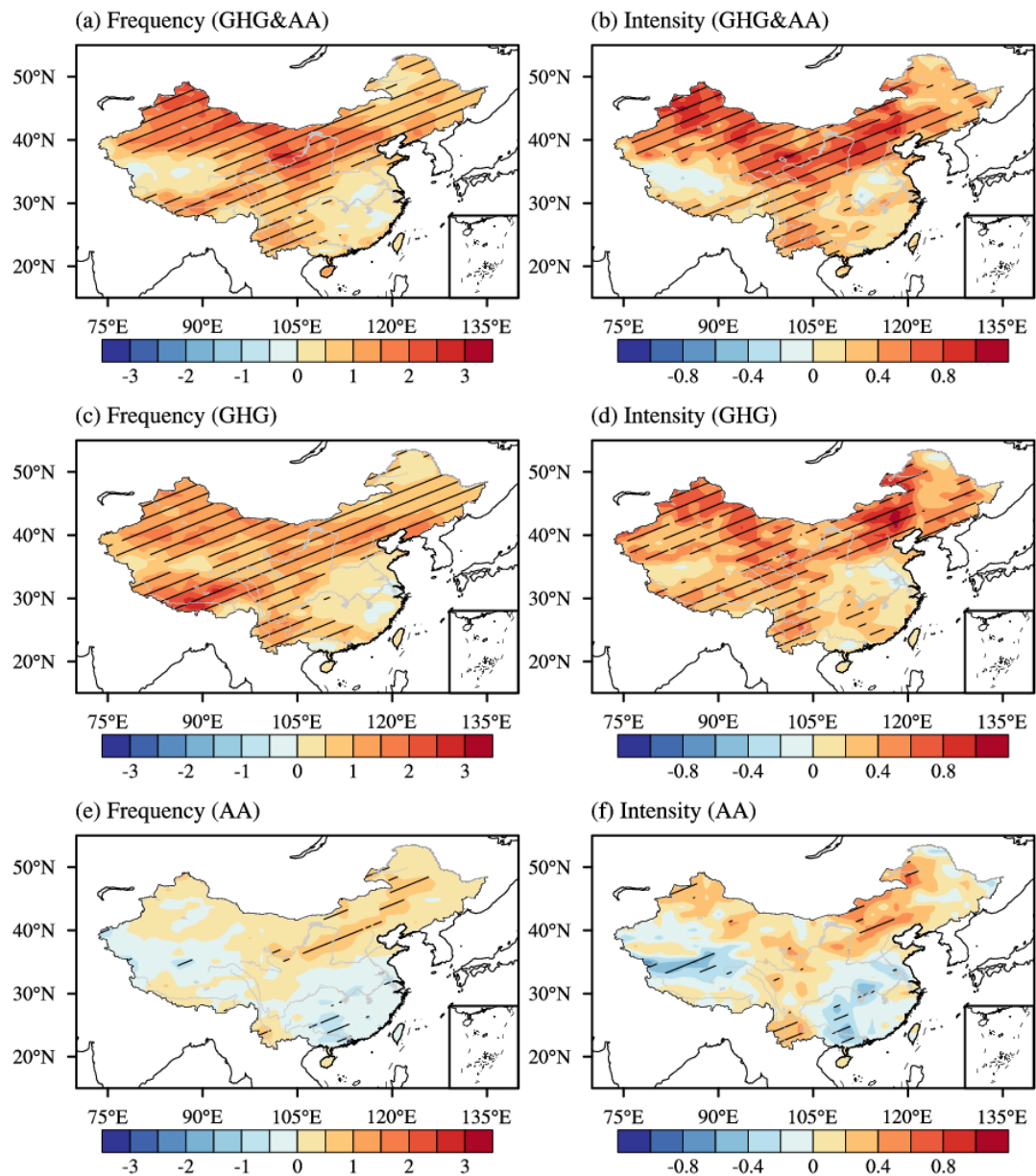
1032 forcing, and (e-f) AA forcing, masked by China boundary. The slashes highlight the regions where

1033 the differences are statistically significant at the 90% confidence level based on a two-tailed Student

1034 *t*-test.

1035

1036

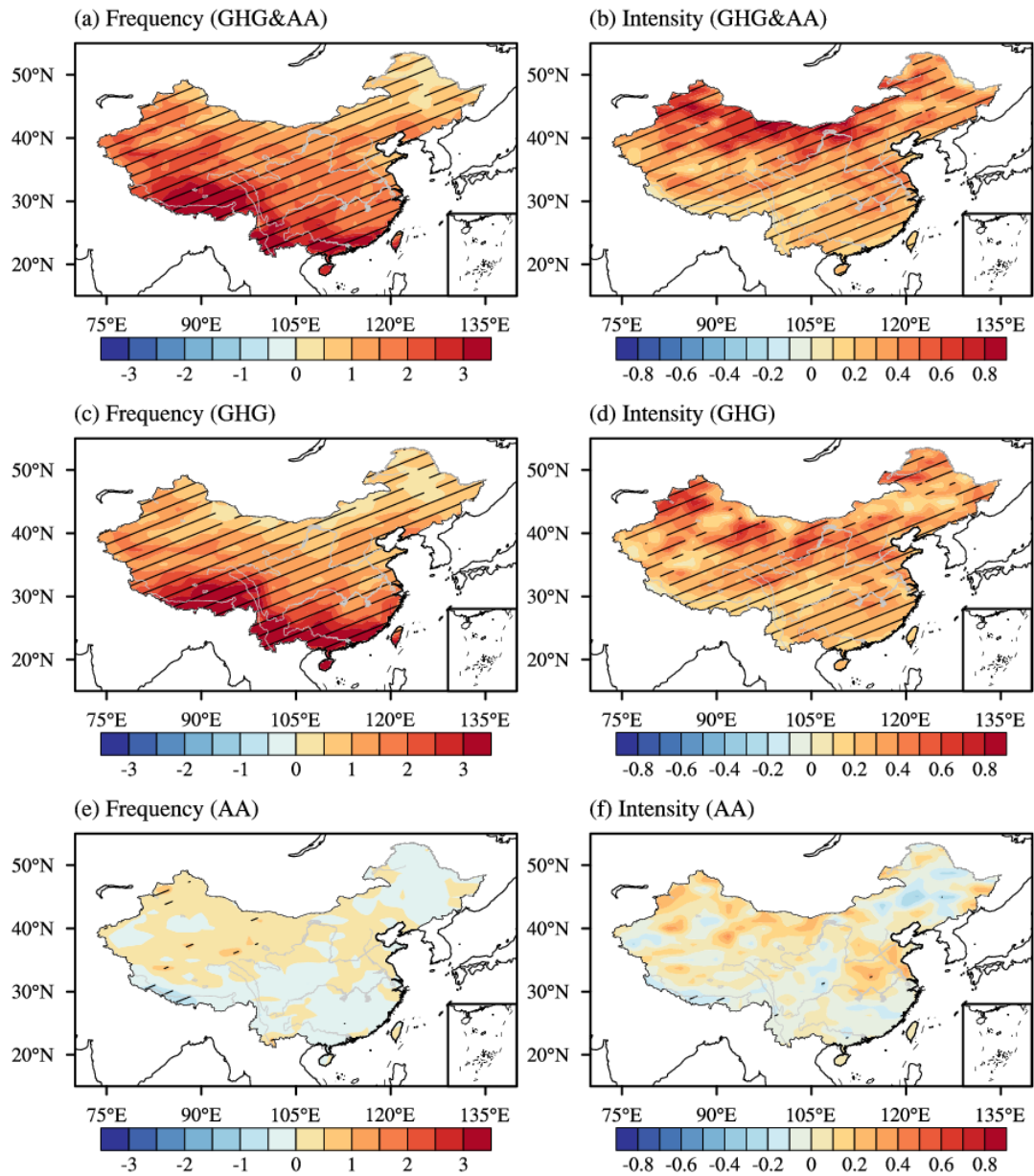


1037

1038 **Figure 5.** Spatial patterns of changes in frequency (units: events/year; left panels) and intensity  
 1039 (units: °C; right panels) of daytime HWs in response to changes in (a-b) ALL forcing, (c-d) GHG  
 1040 forcing, and (e-f) AA forcing, masked by China boundary. The slashes highlight the regions where  
 1041 the differences are statistically significant at the 90% confidence level based on a two-tailed Student  
 1042 *t*-test.

1043

1044



1045

1046 **Figure 6.** Spatial patterns of changes in frequency (units: events/year; left panels) and intensity

1047 (units: °C; right panels) of nighttime HWs in response to changes in (a-b) ALL forcing, (c-d) GHG

1048 forcing, and (e-f) AA forcing, masked by China boundary. The slashes highlight the regions where

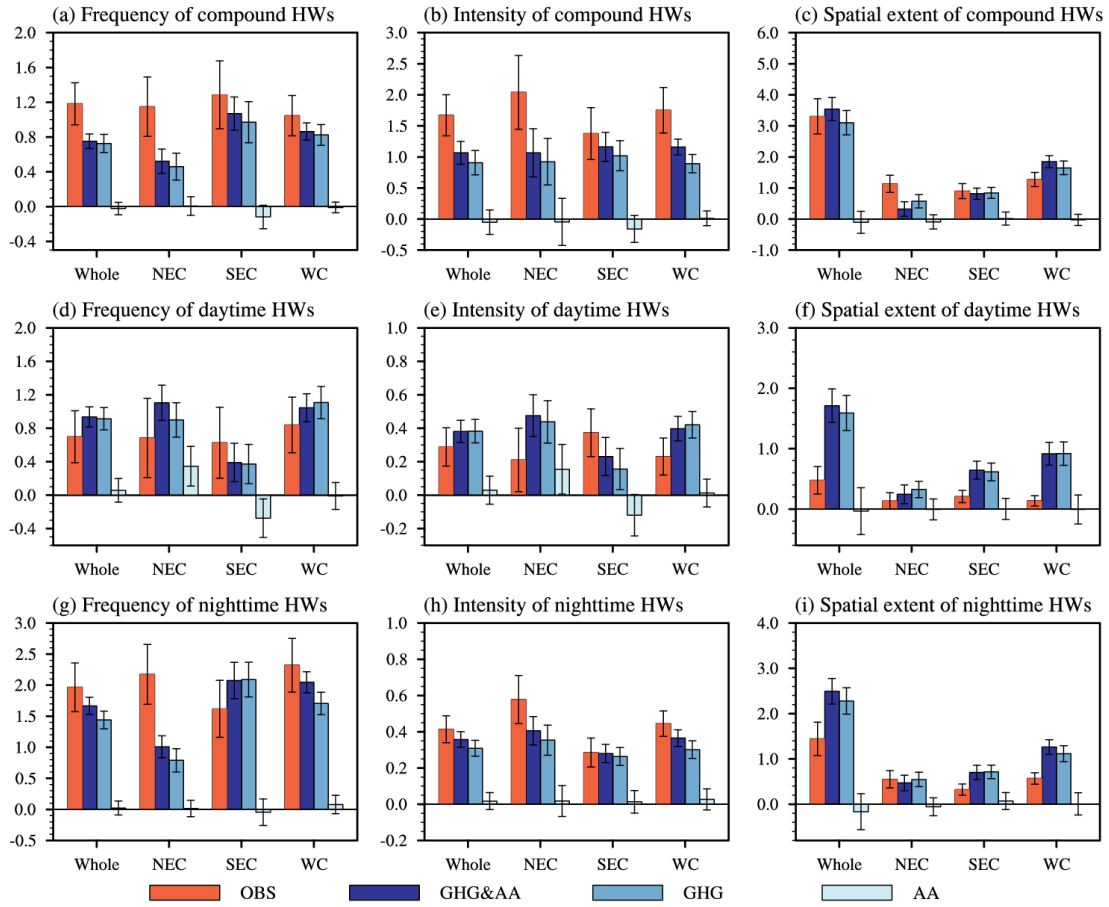
1049 the differences are statistically significant at the 90% confidence level based on a two-tailed Student

1050 *t*-test.

1051

1052

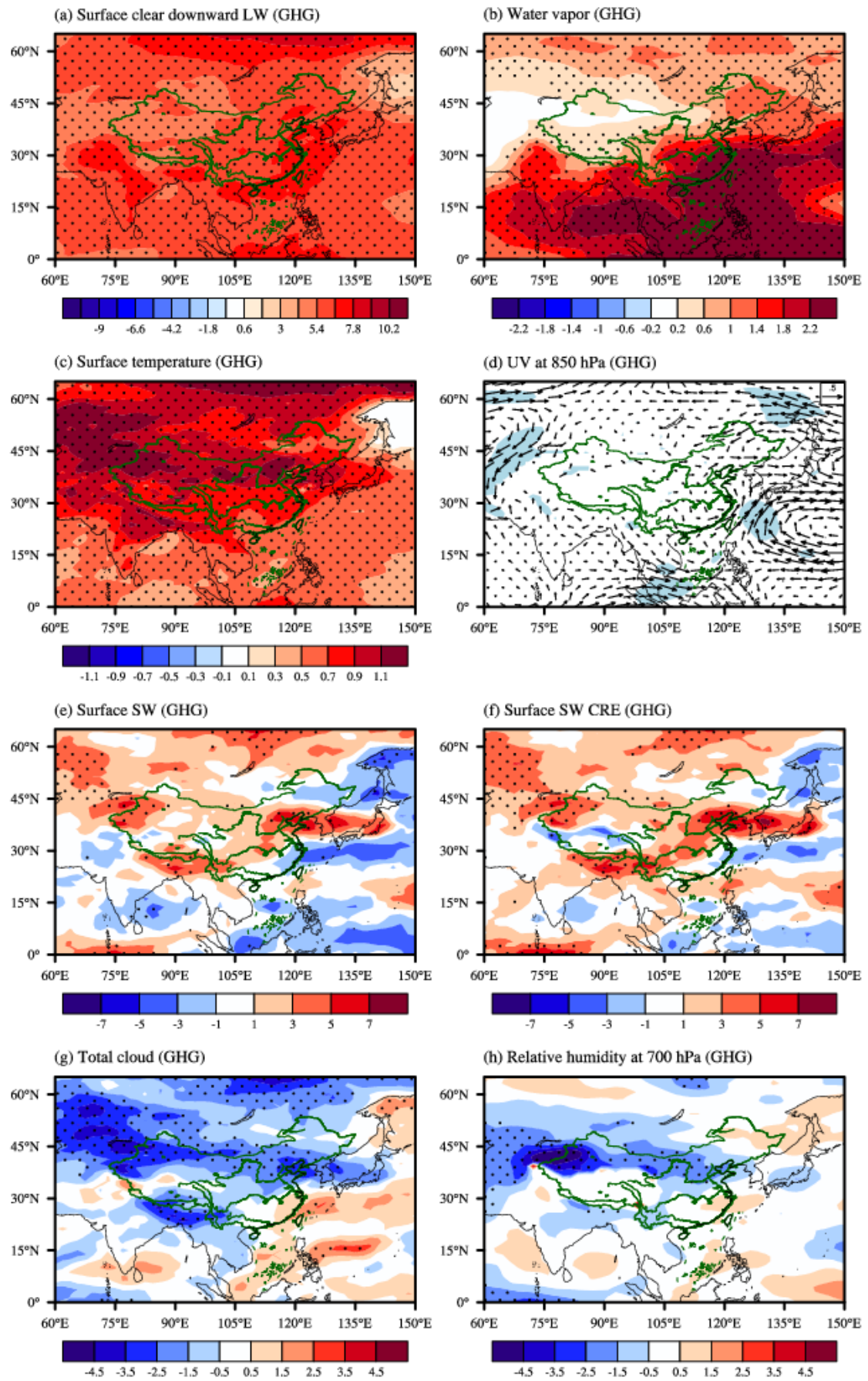




1053

1054 **Figure 7.** Area averaged changes in frequency (units: events/year; left panels), intensity (units: °C;  
 1055 middle panels), and spatial extent (units: 10<sup>6</sup> km<sup>2</sup>; right panels) of (a-c) compound, (d-f) daytime,  
 1056 and (g-i) nighttime HWs over whole China, NEC, SEC, and WC in observations and simulations  
 1057 forced by ALL forcing, GHG forcing, and AA forcing. The error bars indicate the 90% confidence  
 1058 intervals based on two-tailed Student *t*-test.

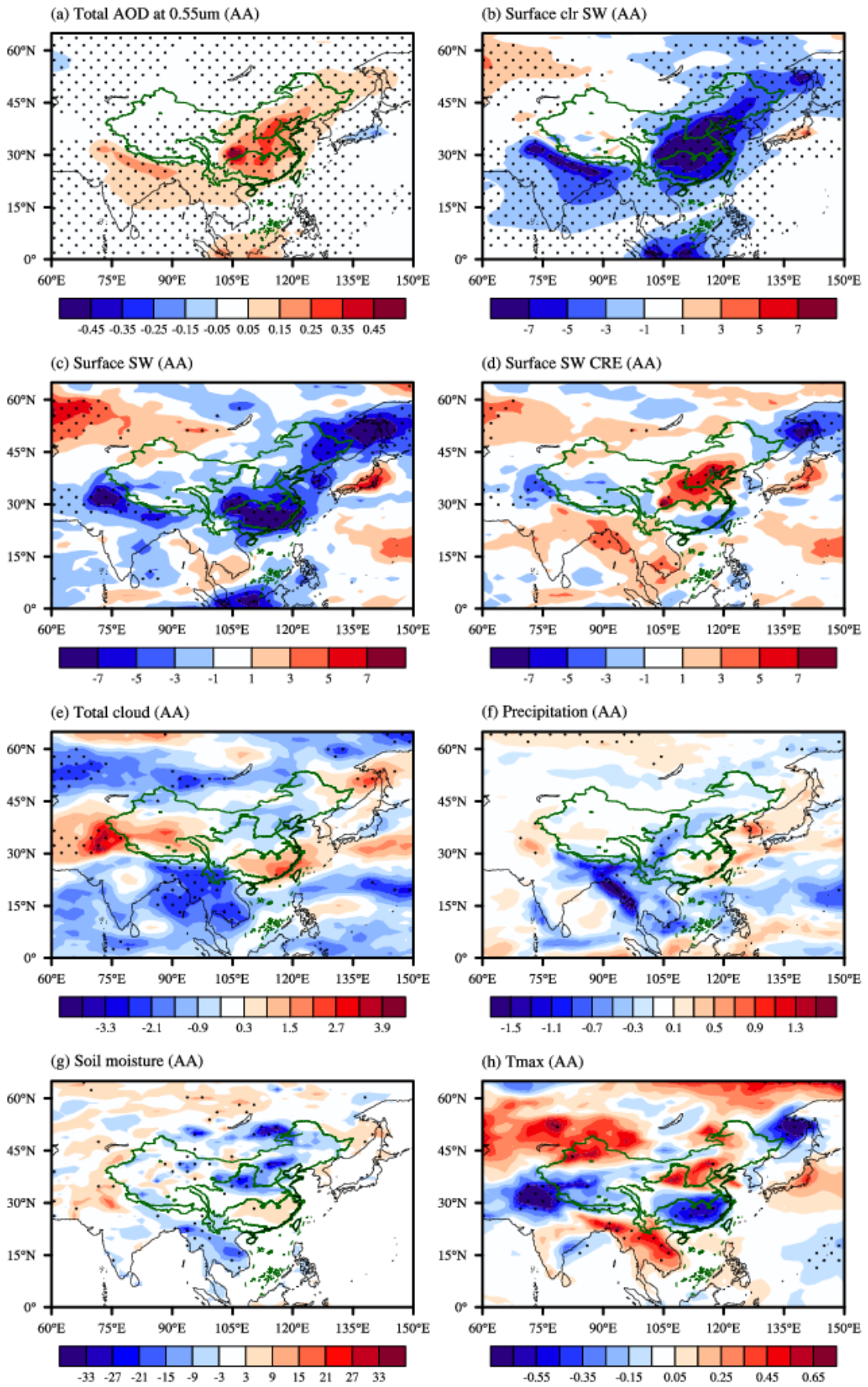
1059



1060

1061 **Figure 8.** Spatial patterns of extended-summer-mean response to changes in GHG forcing (C-PD-

1062 GHG minus C-EP): (a) surface clear sky downward LW radiation; (b) water vapor (units:  $\text{kg m}^{-2}$ );  
1063 (c) surface temperature (units:  $^{\circ}\text{C}$ ); (d) horizontal wind at 850 hPa (units:  $\text{m s}^{-1}$ ); (e) net surface SW  
1064 radiation; (f) surface SW CRE; (g) total cloud cover (units: %) and (h) relative humidity at 700 hPa  
1065 (units: %). Radiation with positive value meaning downward and in  $\text{W m}^{-2}$ . The black dots in a-c  
1066 and e-h and the blue shadings in d highlight regions where the changes are statistically significant  
1067 at the 90% confidence level based on a two-tailed Student *t*-test.



1068

1069

**Figure 9.** Spatial patterns of extended-summer-mean response to changes in AA forcing (C-

1070 PD-AA minus C-EP): (a) total AOD at 0.55  $\mu\text{m}$ ; (b) net clear sky surface SW radiation; (c) net  
1071 surface SW radiation; (d) surface SW CRE; (e) total cloud cover (units: %); (f) precipitation (units:  
1072  $\text{mm day}^{-1}$ ); (g) soil moisture (units:  $\text{kg m}^{-2}$ ) and (h) Tmax (units:  $^{\circ}\text{C}$ ). Radiation with positive value  
1073 meaning downward and in  $\text{W m}^{-2}$ . The black dots highlight regions where the changes are  
1074 statistically significant at the 90% confidence level based on a two-tailed Student *t*-test.

1075

1076